Unfolding IGDQ Peptides for Engineering Motogenic Interfaces

Federica De Leo,† Riccardo Marega,† Valentina Corvaglia,† Simone Silvestrini,‡ and Davide Bonifazi,†,§*

†Department of Chemistry, University of Namur (UNamur), Rue de Bruxelles 61, 5000, Namur, Belgium; ‡Dipartimento di Scienze Chimiche, Università degli Studi di Padova, V. Marzolo 1, 35131, Padova, Italy; §School of Chemistry, Cardiff University, Park Place, Main Building, CF10 3AT, Cardiff, UK. Email: bonifazid@cardiff.ac.uk

Keywords: IGD peptides, molecular modeling, peptide SAMs, chemical gradient, cellular migration, cancer cells.

ABSTRACT: Extracellular matrix (ECM)-mimicking surfaces are pivotal tools for the understanding of adherent cells physio-pathology. In this sense, we have recently reported on a discrete set of ECM-mimicking SAMs, among which only those exposing IGDQ peptide-alkanethiols sustain the adhesion of MDA-MB-231 cells by triggering FAK phosphorylation and peculiarly induce migration of individual cancer cells at the sub-cm scale. Starting from the experimentally observed relationship between the SAM composition, organization and biological

response, a systematic computational characterization aided in pinpointing the atomistic details through which specific composition and organization achieve the desired biological responsiveness. Specifically, solvent, number and type of peptides, the presence or the absence of the surface fillers, were accurately considered creating representative model SAMs simulated by means of classical Molecular Dynamics (MD) in the view of unravel the experimental evidences, revealing how the conformational and structural features of these substrates dictate the specific motogenic responses. Through complementary experimental and computational investigations, it clearly emerges that it exists a distinct and precise way of mutually interact between IGDQ-peptides, the surface fillers and Au, that control the structural properties of the ECM-mimicking SAMs, and thus their motogenic potential.

INTRODUCTION.

Cellular microenvironment is certainly one of the most important components regulating the behavior of cells through biochemical, biomechanical and bioelectrical signals derived from surrounding cells, extracellular matrix (ECM), and soluble factors.[1, 2, 3] These components work in synergistic and antagonistic manners to regulate the cellular behavior, triggering either physiologic or pathologic responses. In this respect, understanding fundamental individual and collective cellular migration mechanisms[4] could in principle help current therapeutic developments in cancer treatment, as the stimulation of malignant cells to migrate allows them undergoing metastatic growth in distant organs.[5] Indeed, when accomplishing fundamental

biological processes, such as adhesion, replication and migration, most mammalian cells must cross-talk with the underlying ECM, a complex meshwork of proteins (fibrinogen, vitronectin, collagen, fibronectin),[6] growth factors (EGF, bFGF, VEGF)[7, 8, 9] and glycosaminoglycans.[10] Among these structures, fibronectin (Fn) occupies a central role in cellular adhesion, growth, and migration.[11, 12] It exists as a protein dimer, consisting of two nearly identical polypeptide chains linked by a pair of C-terminal disulfide bonds.[11] Each Fn monomer has a molecular weight of 230–250 kDa and contains three types of modules: type I, II, and III (Figure 1). All three modules are composed of two anti-parallel β-sheets although only types I and II are stabilized by intrachain disulfide bonds. Following seminal discoveries by *Pierschbacher* and *Ruoslahti*,[13] scientists could establish that the activities of Fn are linked to the action of specific peptide sequences buried into dynamic cryptic sites (Figure 1). In particular, the Arg-Gly-Asp (RGD) peptide, localized in a flexible loop of the Fn III_{10} module,[14, 15] mediates cellular adhesion through the binding to integrin and its action as an independent chemoattractant has been extensively studied both in solution and on artificial interfaces.[16, 17, 18]

More recently, it was also found that a cryptic Fn motif Ile-Gly-Asp (IGD), identified in the I7 and I9 modules of the gelatin-binding domain and in the migration stimulating factor of Fn (Figure 1), induces high motogenicity in human dermal fibroblasts.[19] Following studies also suggested that modified Fn exposing IGD residues are somehow involved in the migration of metastatic cells as a result of a proteolytic modification of the protein.[20, 21, 22, 23]

To probe the motogenic properties of the IGD peptide with model cancer cells, we recently engineered isocratic monolayers and SAM gradients on Au surfaces by chemical co-absorption of tailored thiol-bearing Ile-Gly-Asp-Gln (IGDQ) peptides and molecular fillers.[24]

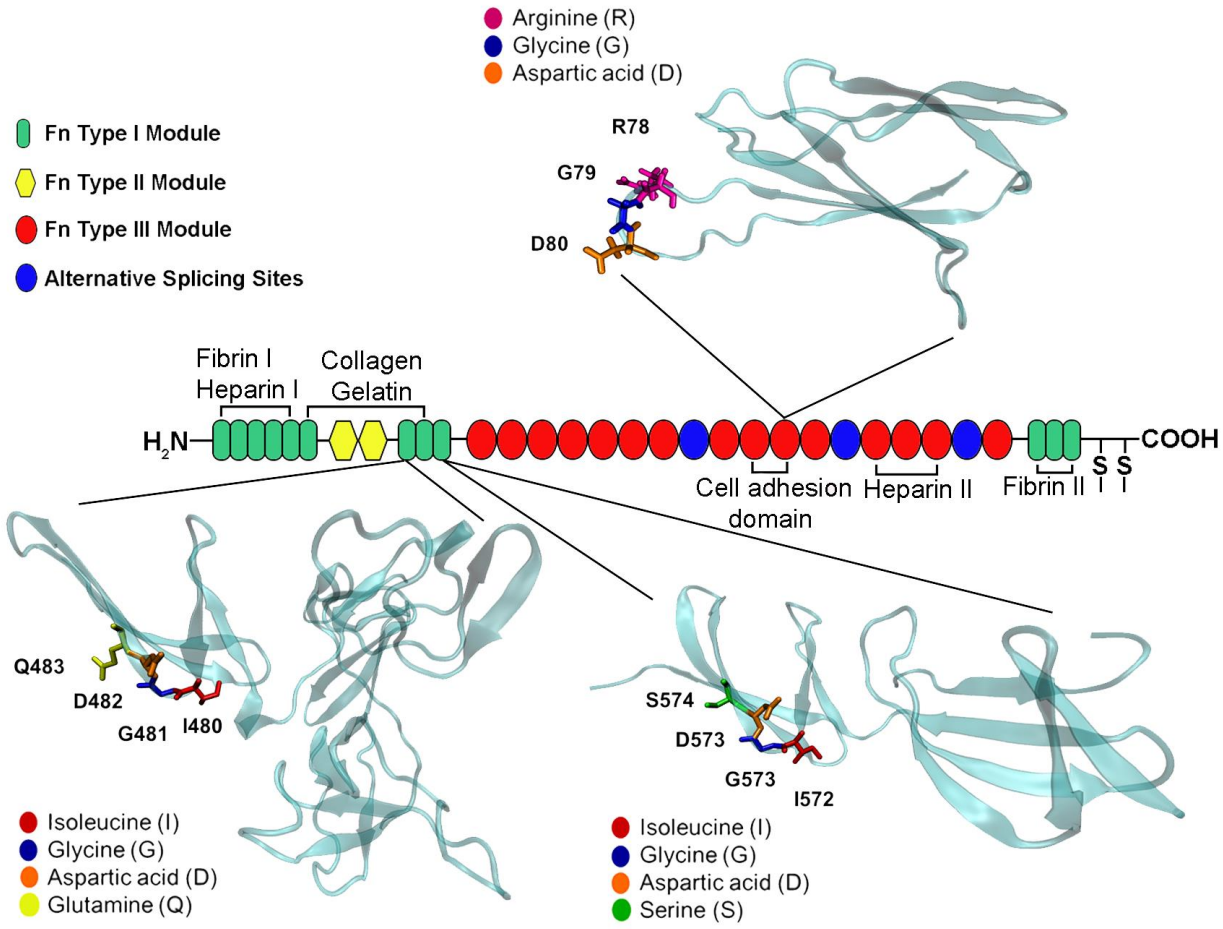

Figure 1. 3D structures of the tenth fibronectin (Fn) type III module containing RGD (PDB 1TTG), sixth and seventh Fn type I modules containing IGDQ (PDB 3MQL) and the eighth and ninth Fn domain pair type I module containing IGDS (PDB 3GXE).

Adhesion and Western blot assessments on the whole-population migration of metastatic breast cancer cells (MDA-MB-231 cells) showed that the IGDQ-exposing SAMs specifically withstand the adhesion of the cancer cells, with the monolayer gradients inducing migration of cell subpopulations.[24] However, when engineering an artificial ECM mimic, one should also consider the static and dynamic properties of both the bioactive peptide ligand structure as well as of the interface where it resides.[25, 26, 27, 28, 29] For instance, interfacial architectures either burying or inducing unfavorable conformations of the ligands, could in principle be biologically silent. Peptides and proteins are among the main tools for the preparation of artificial ECM analogues,[30, 31, 32, 33, 34, 35, 36, 37, 38, 39, 40] but their charged aa sidechains (i.e. those in LYS, ARG, and ASP) display a strong tendency to adsorb onto Au(111) surface through charge transfer interactions.[41] This can influence the orientation of polar groups (such as the peptide bonds, the NH_3^+ groups of LYS, or the COO^- groups of ASP) in the interfacial region, thus affecting its recognition properties.[42] In this respect, several studies recently appeared in the literature describing structure and conformation-dependent adsorptions of polypeptides on Au.[22, 43, 44, 45, 46, 47, 48, 49, 50, 51] The adopted flatten conformations on the surface suggest that molecular fillers (peptidic-[36] or alkylic-spacers and "surface fillers"[30, 36, 52, 53]) populating the underneath area are needed to avoid undesirable surface absorption of the peptide ligand.[22, 30, 36, 42, 43, 44, 45, 46, 47, 48, 49, 50, 51, 53]

Given these premises, in this paper we describe the structural properties that IGDQ-exposing SAMs should have when aimed at triggering cell migration on an artificial interface. In particular, we investigated and clarified how the composition, peptide surface concentration and surface filler presence affect the bioactive ligand orientation, thereby identifying the ideal combination of such

elements for the attainment of responsive IGDQ-exposing interface toward cellular adhesion and migration.

RESULTS AND DISCUSSION

Preparation and physicochemical investigations of IGDQ-exposing SAMs. Following the approach previously described by us,[24] we have prepared through solid-phase peptide synthesis (SPPS) a series of IGDQ-containing molecules (**ISH** and **IPSH)** bearing a thiol anchoring group linked to the peptide termination either through hydrophilic (an undecyl-tetraethyleneglycol chain in **IPSH**) or hydrophobic (an octyl chain in **ISH**) linkers (Scheme 1). We also used surface "fillers", which are alkanethiol molecules composed by either an undecyl-tetraethyleneglycol moiety (**PSH**, mimicking the linker of **IPSH**) or a n-octanethiol core (**CSH**, mimicking the linker of **ISH**). Following a classical one-step full immersion procedure, we generated isocratic SAMs (Table S2 entries 1-8),[54, 55] while through a two-step immersion protocol[56] we realized SAM gradients (Table S2 entries 9-13). We first characterized the SAMs properties by measuring their wettability, through water contact angle assessment (WCA, Table S2), since this technique is well used to elucidate macroscopically the static and dynamic structural properties of SAMs.[55, 57, 58, 59, 60, 61, 62, 63, 64]

WCA measurements define the range of wettability values for all of the surfaces reported in this study. Specifically, WCA values of the SAMs prepared with only the surface fillers (Table S2, entries 1,2) span from 32.4° (for **PS·Au**) to 103.3° (for **CS·Au**). An intermediate wettability value of about 54.3° has been found for **IPS·Au**, the latter exposing only the hydrophilic peptide (Table

S2, entry 3), while surprisingly low values resulted from the surfaces exposing the hydrophobic one (41.7° for **IS·Au**, see Table S2 entry 4). The latter finding may suggest the formation of "amorphous" SAMs, due to limited molecular packing and aspecific adsorption connected to "lying down" peptide alkanethiol conformations,[52] but no further investigations were carried out in this sense since this substrate lack of motogenic activity.[24]

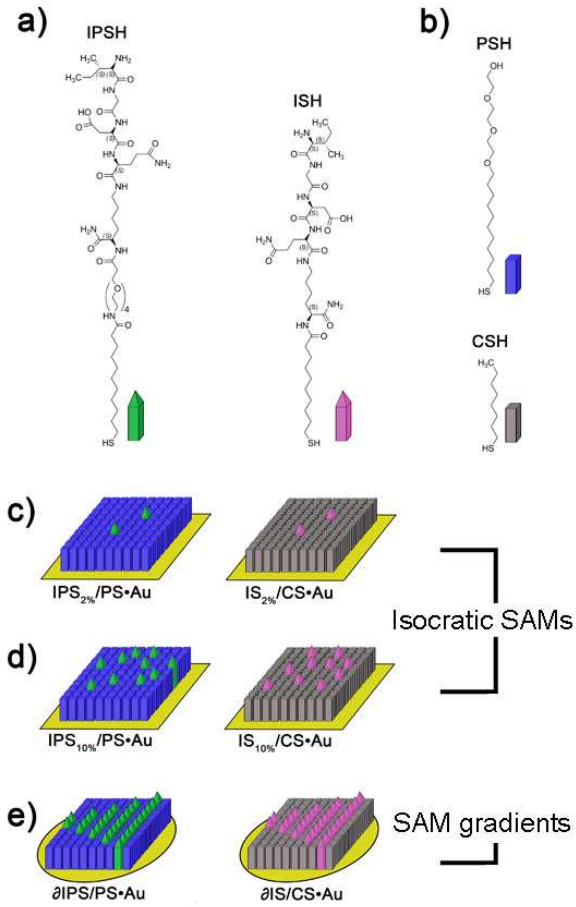

Scheme 1. Schematic representation a) of the peptide-exposing thiol ligands **IPSH** and **ISH**, b) the surface fillers (**PSH** and **CSH**) and of their SAMs on Au surfaces as c,d) isocratic SAMs and e) SAM gradients.

WCA measurements of the set of the substrates exposing both peptide alkanethiol and filler evidence the progressive change of the WCA values as a function of the peptide molar ratio (0, 2%, 10%, and 100%, Table S2, entries 5-8), or the position along the peptide chemical gradient (ca. 3, 6 and 9 mm, Table S2, entries 9-12). For instance, the group of SAMs exposing **IPSH** and **PSH** shows hydrophobicity increase (from 32.4° to 54.3, Figure 2a), while those surfaces covered with **ISH** and **CSH** display an opposite trend (from 103.3° to 41.7°, Figure 2a).

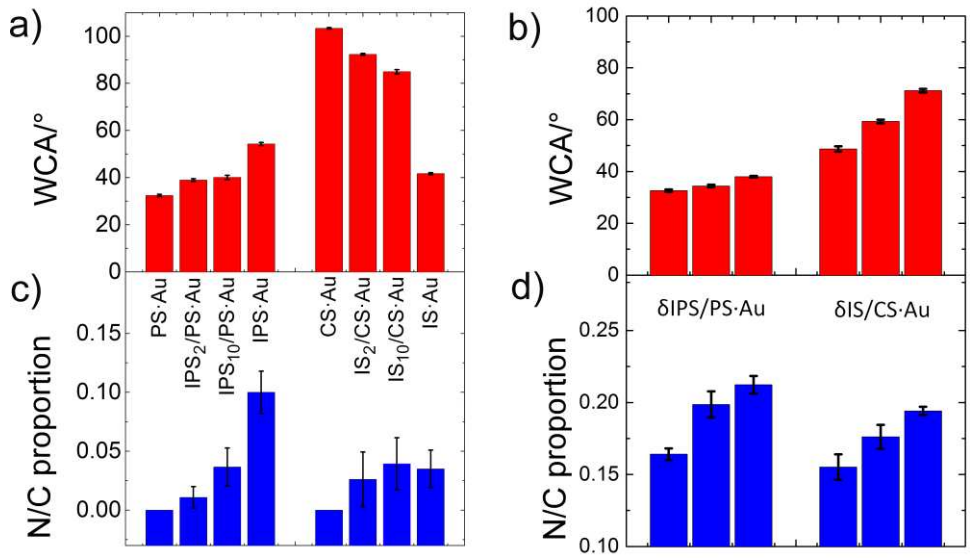

Figure 2. Relation between the peptide molar ratio and (a,b) wettability or (c,d) peptide density (expressed as N/C at% proportion) as revealed by WCA and XPS assessments on the (a,c) set of isocratic SAMs and (b,d) SAM gradients. For the SAM gradients, the water droplets were delivered at the beginning, mid and end of the chemical gradient (ca. 3, 6 and 9 mm along the direction of the chemical gradient). WCA and N/C values corresponding to these positions in the chemical gradients are expressed by the left, mid and right column in plots (b,d). Values are reported as mean Y±S.D.

Regarding the SAM gradients, the WCA values clearly reveal the anisotropic wettability of these ECM-mimicking substrates (Table S2, entries 9-13, and Figure 2b), which show that the hydrophobicity increases along the versus imposed by the gradient concentration. Indeed, WCA values variation (ΔWCA) ranges from 5.4°, for the hydrophilic SAM gradient **∂IPS/PS·Au** (Table S2 entry 9 and Figure 2b), to 22.5° for the hydrophobic SAM gradient **∂IS/CS·Au** (Table S2 entry 10 and Figure 2b). These results clearly evidence the differences in the wettability between SAMs and SAM gradients, most likely ascribable to the different SAM composition along the gradient direction, the latter affecting the structural organization. As a way of comparing the surface composition of both SAMs and SAM gradients, we studied the surface concentration of the peptide heads (peptide density), by X-ray Photoelectron Spectroscopy (XPS).[65] The elemental compositions and survey scans are reported in Supporting Information S3, where one can clearly see that the nitrogen signal is decreasing in intensity (and thus atomic percentage, at%) moving from the homogeneous isocratic SAMs (IPS·Au, IS·Au and GPS·Au, N at% ≈ 2 – 6%) to those prepared under reduced peptide-to-filler molar ratios ($IPS_{2\%}$/PS·Au, $IS_{2\%}$/CS·Au and $GPS_{2\%}$/PS·Au, 0 < N at% > 2, Supporting information Figure S3-1-15). The set of isocratic SAMs shows marked differences in terms of molecular composition and organization (i.e. thiols length, surface composition and organization), and therefore the Au at% can vary in a broad range of values (i.e. ≈ 67 At % in CS·Au and ≈ 37 at% in GPS·Au, Supporting Information S3-15). Therefore, the best way to compare the differences in the organic moieties of the set of the isocratic SAMs is to normalize the at% of the organic moiety by the Au amount (see supporting S3) and then use the normalized N1s at% and C1s at% (N/C proportion) as indicator of the peptide density. In the case of the SAM gradients the peptide density is changing within the same sample, the Au

at% is rather constant and the signals originating from C, O, and S result from the specific composition between peptide and filler. In this case, the at% normalization is done by the Au at%, yielding gradually increasing N1s/Au4f at%, almost steady S2p/Au4f, and complex trends for C1s/Au4f and O1s/Au4f (see Supporting Information S3-20-22). As expected, the peptide density increases as a function of the peptide molar ratio (Figure 2c), while it raises following the distance along the chemical gradient in the set of SAM gradients (Figure 2d). In the latter case, the linear relation between the nitrogen content and the position along the surface unambiguously confirms the anisotropic peptide distribution of these ECM-mimicking substrates (0.58, and 0.55 N1s at% mm^{-1} for ***∂*IPS/PS·Au** and ***∂*IS/CS·Au**, respectively, see Figure 4a and Supporting Information S3-20-22). The structural properties of isocratic SAMs and SAM gradients can be further compared by linking the WCA values and the peptide density. In the isocratic SAMs, the change in the properties between the substrates surfacing 0% peptide (i.e. **PS·Au** and **CS·Au)** to 100% peptide (i.e. **IPS·Au** and I**S·Au)** could somehow relate to the changes in the surface composition in the corresponding SAM gradients (Figure 2). However, both SAM gradients display lower WCA variations and higher values of peptide densities than the corresponding set of isocratic SAMs. Indeed, the WCA values range from 32.6° to 38° *versus* 32.4° to 54.3°, while the N/C at%, result 0.15-0.20 *versus* 0-0.1 (for SAM gradient and isocratic SAMs, respectively). These trends of wettability and peptide density highlight the main effect of the two SAM preparation procedures in terms of SAM composition. SAM gradients clearly display higher peptide-to-filler ratios than the corresponding isocratic SAMs, most likely due to the known differences of both kinetics and thermodynamics of the SAM formation during one step and two-step chemisorption.[66] Nonetheless, these properties may reflect differences in the organization of the surface-bound

peptides (i.e. spacing and conformation consequent to the different surface composition). To better elucidate the order/disorder of the motogenic SAM gradient, we have performed a series of AFM characterizations (air, room temperature) and dynamic WCA measurements on ultra-flat Au(111). As we did for the other chemical and biological characterizations, we have used two isocratic SAMs (IPS10%/PS·Au and IPS90%/PS·Au) as possible representative systems for the interpretation of the morphology in the different areas of the SAM gradient ∂IPS/PS·Au. In a first instance, we performed these experiments exactly on the same kind of substrates used for all the other biological and physicochemical characterizations (15 mm round glass cover slips coated with 100 Å of Au over a 20 Å titanium layer, 0.13-0.16 mm thickness from Platypus Technologies). However, the AFM characterization of these substrates reveals their high surface roughness (See Figure S4-1), which impedes a clear morphological discrimination between the different SAMs. We thus used the Platypus Ultra-Flat Gold Chips, characterized by higher surface homogeneity and larger areas of Au (111) terraces compared to the other kinds of substrate (See Figure S4-1). Furthermore, while the former Au substrate required an acidic and ozonolytic pre-treatment as described in the experimental section, these ultra-flat chips (from now on uf-Au(111)) are ready to use with no cleaning procedure.

Consequently, we expected different properties between these two kind of substrates before and after SAM formation (i.e. roughness, order, wettability). Tapping mode AFM characterization on relatively large areas (5 – 25 μm2) of the isocratic SAMs (Figure S4 1-3) clearly shows the presence of soft matter chemisorbed onto the Au surface, with objects having height values spanning from 1 to 7 nm, thus compatible with the length of the organic molecules used for the

chemisorption (about 5 and 2.6 nm, for the IPSH peptide and the PSH filler in their extended conformation, respectively). By looking at the morphology and the cross-section values onto smaller areas (0.25 – 1 μm^2, Figure S4-3 to 7), one can clearly appreciate the difference between ultra-flat Au and the SAMs, and between the SAM exposing "low" IPSH density (IPS10%/PS·Au) and the other one (IPS90%/PS·Au). For the characterization of the SAM gradient ∂IPS/PS·Au, we report the results from the AFM imaging over large (225 μm^2), medium (4 μm^2) and small (0.25 μm^2) areas, which sustains the presence of an anisotropic distribution of soft matter and sheds light on the molecular packing of the peptide and the filler across the anisotropic substrate. The imaging across large areas (225 μm^2, Figure S4-7) shows the presence of small "hills" of organic matter, whose density seems to diminish along the direction of the chemical gradient. The analysis of 4 μm^2 areas (Figure S4-8) reveals that these small aggregates display a broad range of height values (3 -20 nm), with some of them fitting with the theoretical length values of the chemisorbed thiols, and a part of them clearly representing aggregates of organic matter.

Morphology and phase imaging on the small areas (0.25 μm^2, Figure S4-9) not only confirm the aforementioned findings, but also suggest that in the high-density region, the molecular packing results much higher than the low-density region, as seen by more homogeneous cross section profiles and phase contrast. Taken together, these results suggest that the morphology of the ∂IPS/PS·Au SAM is deeply governed by the kinetics of the IPSH chemisorption during the gradient preparation. We hypothesize that in the portion of the substrate that is less exposed to IPSH (low-density region), the peptides chemisorb messily through small aggregates observed as "patches" on the Au surface. On the other hand, regions that undergo immersion time of 15 min

result in high density regions as the IPSHs have longer time to optimize the occupied space in an organized monolayer with increased peptide amount (in line with the nitrogen levels revealed by XPS assessment). The new WCA measurements onto these uf-Au(111) chips yield static WCA of 31° for IPS10%/PS·uf-Au(111), of 55° for IPS90%/PS·uf-Au(111), of 64° and 51° for the ∂IPS/PS·uf-Au(111) in the low- and high-density regions, respectively. While the WCA values of the isocratic SAMs previously obtained are now nicely reproduced on the uf-Au(111) chips, those of the gradients significantly differ both in absolute values and wettability change across the gradients according to the kind of substrates. Concerning the absolute values, their differences might be explained by the baseline (WCA of the clean substrate) registered that was close to zero for the former Au substrates, while was 40 – 50° for the uf-Au(111) chips. On the other hand, the difference in the wettability variation along the gradient (+5° for the former Au substrates and -13° onto the uf-Au(111) chips) can be explained by the different surface roughness: the rougher Au substrate can facilitate the adsorption of the filler, smaller in size, rather than the peptide aggregates. In that scenario, the amount of filler molecules in the low-density region of the gradient can influence the peptide packing in a substrate rather than in the other.

The differences between the static WCA values of the isotropic SAMs and the SAM gradient onto uf-Au(111) chips is probably due to the highly kinetic character of the anisotropic patterning consequent to the two step immersion protocol. Static WCA of ∂IPS/PS·uf-Au(111) shows values from around 65° (low-peptide region) to 50° (high-concentration region). The low peptide concentration region could present the chemisorbed peptide in a flat conformation, reducing the Au sites available for the chemisorption of the filler, thus diminishing its contribution towards

hydrophilicity. This is in line with the large number of aggregates observed per μm^2 in the AFM characterization (see Figure S4-8-9). Regarding the high concentration region of SAM gradient, the wettability can be compared to the one of the isocratic IPS90%/PS·uf-Au(111) SAM, where the contact angle is about 50°. These results can be explained by considering that the gradient is pretty shallow also onto these ultra-flat chips, as confirmed by XPS analysis (data not shown), and considering the very kinetic character of the thiol self-assembly. The difference in thiol adsorption can play an important role in the second immersion step, where the "gentle" backfilling conditions (μM concentration of the filler and reduced immersion time) should promote surface saturation and avoid massive peptide replacement. Having an already saturated surface of perhaps flat peptide, this can lead to a small increase in hydrophilicity (ΔWCA of -15°). Regarding the dynamic measurements, advancing and receding contact angle measurements (ARCA, see Figure S4-10) $IPS_{10\%}$/PS·uf-Au(111) ARCA shows an advancing WCA of 39° and a receding WCA of 30°. The ARCA WCA difference is 8° indicating that the system is well packed, with just 10% of peptide in the isocratic SAM. $IPS_{90\%}$/PS·uf-Au(111) ARCA shows an advancing WCA of 62° and a receding value of 29°. The difference is 32°, which shows that increasing the percentage of peptide, leads to the addition of local disorder due to the peptide organization. ∂IPS/PS·uf-Au(111) ARCA measurements in the low-density region show an advancing value of 72° and a receding angle of 53°. The difference in angles is 19°. This can be due to an intermediate situation in which some peptide stays flat or is bound as aggregates across the surface, leading to local disorder.

∂IPS/PS·uf-Au(111) ARCA measurements show and advancing value of 67° and a receding angle of 42°. The difference between such values is 25°, showing probably that despite the lack of

aggregates seen in the AFM analyses, the packing is still far from the isocratic self-assembly where homogeneity is considerably higher. The higher hysteresis value of 25° is due to the higher peptide concentration on surface. Increasing the peptide concentration decreases the homogeneity of the packing even if no aggregates can be found in the high concentration regions of the AFM surface analyses. Based on the wettability and XPS findings, one may conclude that one step- versus two-step procedures generate distinctly-organized ECM-mimicking substrates, whose differences are not limited to the peptide density, but most likely reflect the different structural organization.

Taken together, these data confirm that the SAM organization strongly depends not only on the overall composition, that is the presence of the IGD-bearing peptides, the alkanethiol fillers, the Au surface, but also on the chemisorption procedure. It can be plausibly inferred that such different SAM organizations might be governed by intercomponent interactions affecting the peptide adsorption onto Au, its conformational freedom and ultimately its orientation.

Biological activity of the ECM-mimicking SAMs. For the biological studies we selected cell lines displaying different level of integrins (key cell-surface receptors involved in the transduction between extracellular *stimuli* and cytoskeleton rearrangements),[12, 67, 68] and thus capable of undergoing migration (physiologically- or pathologically-driven). For the whole study, we focused on the MDA-MB-231 cells, which are a known model of metastatic breast cancer cells, and used human dermal fibroblasts (HDF) and MDA-MB-435 cells (model of melanoma cells) as controls.

In the first step, we have performed adhesion assays at both cellular and molecular level to evaluate whether SAMs exposing the IGD motif can sustain cell adhesion, which is the prerequisite for migration and replication. Adhesion of MDA-MB-231 cells at the whole-population level was screened by a standard assay, which involves the cell seeding, incubation and gentle washing to remove the loosely bound cells over the substrates.[24, 30, 69] By combining such method and optical microscopy imaging (Supporting information S1), a dataset of cell densities was generated, allowing for the determination of the cell adhesion percentage (CA%) on every tested SAM. Adhesion at the molecular level was instead evaluated by determining the FAK expression and phosphorylation level (pY397-FAK/FAK ratio).[70, 71, 72] The biological dataset of CA%, FAK expression and phosphorylation can be put in relation with the surface properties emerging from the wettability (WCA) and peptide density (N/C proportion) assessments of the different SAMs (Figure 3c-f). One can notice that a broad range of WCA values and N/C proportions elicits high cell adhesions (i.e. more than 60%, Figure 3a-b). On the contrary, the lack of the peptide moiety in the control SAMs appears the main reason for the lower percentages detected. The influence of WCA and N/C proportion on the FAK expression sustains these findings, since all of peptidic-SAMs elicit higher expression levels (≈ 2- to 10-fold) than the bioinert PS·Au substrate. Conversely CS·Au SAM triggers non-negligible FAK levels most likely due to aspecific hydrophobic interactions (Figure 3c-d). Thus, the presence of the bio-specific peptidic moiety is the mandatory requirement to elicit specific cell adhesion both at whole population and molecular levels, excluding an aspecific effect mediated by the mere physicochemical properties of the SAMs understudy. Remarkably, the SAMs exposing the IGD motif induce high FAK phosphorylation (0.5 – 0.9, Figure 3e-f), similarly to the reference surfaces exposing RGD peptides

(Figure 3e,f). These results suggest that, regardless of the surface wettability, cell-adhesive SAMs require the IGDQ termination to sustain specific cell adhesion. We have then developed a test to reveal whether these ECM-mimicking SAMs can trigger motogenic responses on the MDA-MB-231 cells. To this aim, we patterned the SAM gradients by xurography,[24] to delimit the cell deposition spot (a round area of ca. 13 mm^2) and the migration path (rectangular channel of 1 x 9 mm, Supporting information S5).

Regarding the SAM gradients, we observed significant cell displacements by using either ***∂*IPS/PS·Au** or ***∂*IS/CS·Au**, and only cell adhesion and replication in the following conditions: i) SAM gradients lacking of either the surface filler (i.e. ***∂*IS·Au**, Table S2 entry 12) or the IGDQ sequence (i.e. ***∂*CS·Au**, Table S2 entry 13); ii) in the presence of shallower IGD SAM gradients (i.e. ***∂*IPS/PS·Au** prepared with a slower immersion speed, see Table S2 entry 11).

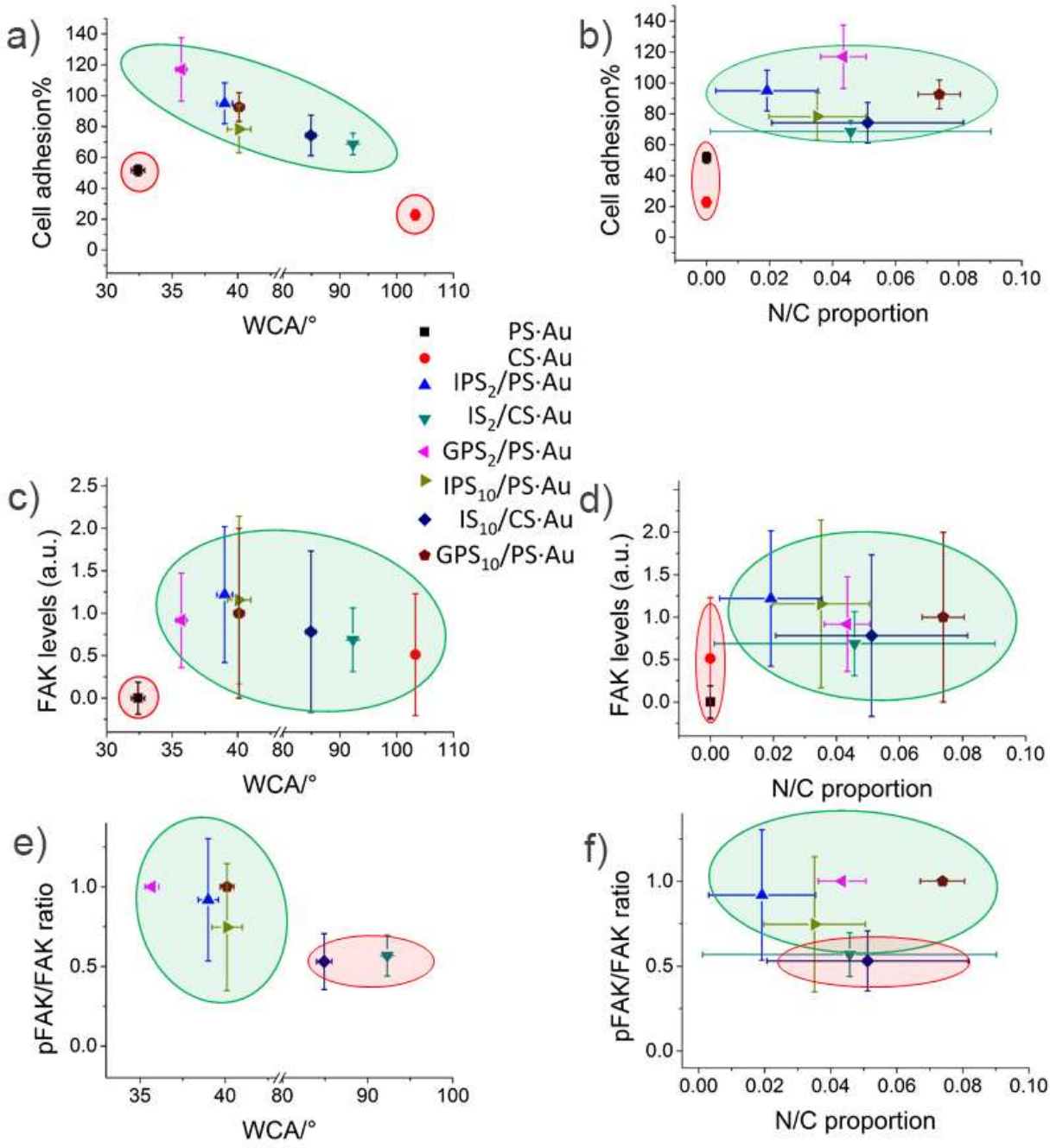

Figure 3. Influence of WCA values (left column) and N/C proportions (right column) of the set of isotropic SAMs in determining the cell adhesion percentages (CA%, a,b), the FAK expression levels (c,d), and the pFAK/FAK ratios (e,f). Data are reported as mean Y±S.E.M and mean X±S.D.

Circles surrounding the data points are meant just to highlight and "sort" the differences between the biologic activity of the peptidic SAMs and those exposing only the fillers (a-d) or between hydrophilic and hydrophobic peptide SAMs (e,f).

For these data, it is clear that the increase of hydrophobicity is not the driving force for the observed cell displacements, since the reference SAM **∂CS·Au** is devoid of motogenicity compared to **∂IS/CS·Au**, despite the similar wettability variations (ΔWCA of 13.3° and 22.5°, respectively, see Table S2). The time-dependent migration of the MDA-MB-231 cells occurs only onto SAM gradients with a defined variation of the IGD surface density (see the ΔN 1s/ΔX values in Figure 4). This suggests that both **∂IPS/PS·Au** and **∂IS/CS·Au** SAMs possess the peptide sequence, anisotropic peptide distribution (about 0.5 ΔN1s/ΔX, see Figure 4), and peptide density (0.15 to 0.23, see Figure 2d), to correctly expose the IGD sequence at the biological interface, ultimately triggering gradient-driven motogenicity.

Due to the nature of the *N*-terminal aa in the IGDQ sequence, proper ILE orientation would therefore relate with the hydrophobic character increment (ΔWCA) of the motogenic surface, as observed by wettability measurements. The motogenic SAMs display changes of the WCA values across the gradients (from 32.6° to 38.0° for **∂IPS/PS·Au** and from 48.7 to 71.2° for **∂IS/CS·Au**, see Table S2). This positive variation of WCA indicates the transition from a more hydrophilic to a more hydrophobic surface, independently of the underneath surface composition (hydrophilic **∂IPS/PS·Au** or hydrophobic **∂IS/CS·Au**). Such hydrophobicity raises cannot be merely associated with the changes in the peptide-to-filler ratios, but may rather reflect the occurrence of

conformational rearrangements, such as a better exposition of the IGDQ peptide hydrophobic portion (the ILE residue) to the aqueous interface.

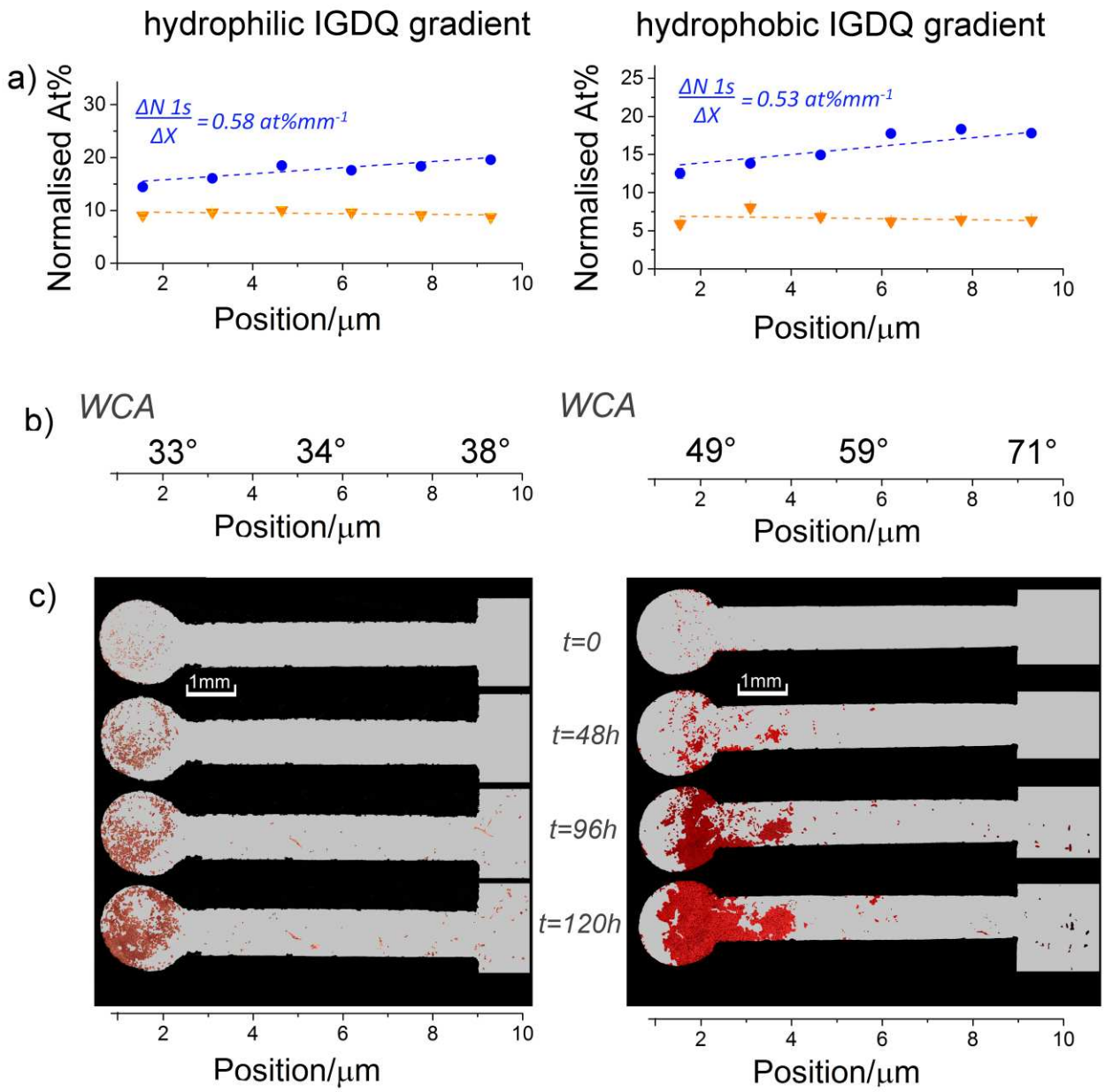

Figure 4. Chemical composition and motogenic properties of SAM gradients: ∂IPS/PS·Au (left column) and ∂IS/CS·Au (right column). a) Position-dependent composition reported as N1s (blue circles) and S2p (orange triangles), at% as revealed by XPS analysis and data normalization (see Supporting Information S3), b) position-dependent WCA values (positioned above the approximate location across the chemical gradient), and c) time-dependent (t=0 – 120h) imaging of the whole-population cell migration across the chemical gradients.

Indeed, SAM gradients devoid of motogenic activity display either a lower hydrophobicity (the WCA along the shallower **∂IPS/PS·Au** change from 30.6° to 34.5°) or even a decrease of the hydrophobicity along the gradient (ΔWCA for **∂IS·Au** is -4.9°). These observations clearly suggest that the abovementioned relationship between the structural composition and organization of the SAM is also related to the motogenic properties exerted at the interface. Additionally, SAM composition and organization bring with them hidden information about the interactions occurring within the SAMs, which might play a role in determining the correct exposition of the motogenic sequence, at last connected to the motogenic effect. Hence, the so inferred structure/activity relationship, although plausible, misses of the structural arguments governing such macroscopic physicochemical properties. Therefore, further studies are required. Aiming at this, a stepwise *in silico* approach was envisaged and carried out to unravel the structural aspects and the interactions at the atomistic level ruling the formation of the correctly exposed IGDQ SAMs.

Theoretical simulation of the IGDQ-confined SAMs. The selected model systems herewith simulated are: *i*) peptides **ISH** and **IPSH** prior to the chemisorption in solutions; *ii*) peptides confined onto the Au surface, in the following environments: one peptide (**1-IS·Au** and **1-IPS·Au**),

two adjacent peptides (**2-IS·Au** and **2-IPS·Au**), and an anisotropic peptide distribution (30 peptides distributed in seven lines in a triangular pattern from one peptide (first line) to seven peptides (seventh line)) mimicking the peptide surface gradient (***∂*IS·Au**, and ***∂*IPS·Au**); *iii*) peptide alkanethiols adsorbed onto Au surfaces as *mixed* SAMs with surface filler onto the Au surface with one peptide (**1-IS/CS·Au** and **1-IPS/PS·Au**), two adjacent peptides (**2-IS/CS·Au** and **2-IPS/PS·Au**), and an anisotropic peptide distribution (30 peptides distributed in seven lines in a triangular pattern from one peptide (first line) to seven peptides (seventh line)) mimicking the peptide surface gradient (***∂*IS/CS·Au** and ***∂*IPS/PS·Au**).

From the solvent to the number of peptides, from the presence to the absence of the surface fillers, every simulated condition is built up in the view of representatively describe and unravel the experimental evidences. In particular, 10 ns classical MD simulations of each system were first run in explicit MeOH, to describe the intra- and inter-molecular interactions potentially occurring during the chemisorption step, followed by additional 10 ns MD simulations in explicit water, to reproduce the conditions potentially occurring at the biological interface with the cells. The choice of simulating three separated systems with a different number of peptides or a peptide gradient-patterned surface originates from the need of understanding the intra and inter-relationships between each IGDQ-based peptide with the Au surface as a function of its increasing concentration. By simulating the presence or the absence of the surface fillers, we aimed at understanding the effect of the filler on the peptide conformation and exposition. All the systems are summarized in Table S7-1.

Generally, both **ISH** and **IPSH** are structurally characterized by a protonated terminal ILE (NH_3) and deprotonated ASP (COO^-) which might represent inter and intramolecular reactive points. Moreover, the presence of the alkyl or ethylene-glycolic linkers might be at the base of backbone flexibility of the two designed peptides. Either aspect might significantly affect the **ISH** and **IPSH** dynamic in solution as well as once chemisorbed onto the Au surface, thus requiring preliminary investigation of their conformational space first in solution. In particular, the structural changes over the MD trajectories were quantified by calculating the Root Mean Square Deviation (RMSD) of the C_α, N and C atoms of the peptides backbone as a measure of the different peptide conformations, by the Radius of Gyration (Rg), which refers to the peptide compactness, and by the peptides H-bonds as indication of the intramolecular interactions possibly occurring after the peptide conformational changes (Figure S7-1).

The two peptides start differentiating already with the <RMSD> analysis that reveals large fluctuations (4.4 ± 0.9 Å) for **ISH** molecule and a more stable profile for **IPSH** (1.5 ± 0.4 Å, Table 1 and Figure S7-1a). The suggested high degrees of freedom associated to the **ISH** conformation, indeed correspond to its alternation between a closed and extended conformation (Figure S7-1a), as demonstrated by cluster analysis (occupancy of the 35.7 % and 64.3 %, respectively). Conversely, **IPSH** tends to preferentially adopt a unique closed conformation (99.7% of occupancy). In line with this, the calculated Rg of **ISH** and **IPSH** initially decreases when the peptides adopt the more compact conformation (closed, Rg_{min} = 5.0 Å for **ISH** and 6.6 Å for **IPSH**), whereas it increases when the molecule switches to the extended structure (Rg_{max} = 8.7 Å for **ISH** and 13.8 Å for **IPSH**, Table 1), showing Rg values oscillating between the two

conformations as a function of time (Figure S7-1b). The comparison of the **ISH** and **IPSH** dynamics laid out already at this stage a different scenario: in MeOH solution **ISH** alternates between two conformations in contrast to the more conformationally stable **IPSH** that is found in a closed conformation. This is essentially driven by the presence of intramolecular H-bonds occurring between the GLN and ASP, ILE and LYS residues that, with a 62 % and 12 % of occupancy respectively, hold the peptide in a closed conformation. Conversely no intramolecular H-bonds have been detected along the trajectory for peptide **ISH**. From these data we can speculate that **ISH** and **IPSH** peptides in solution before approaching the Au surface for the SAM formation would be dominated by significant backbone flexibility and by a considerable H-bonding tendency, respectively. Finally, the Rg values detected for the closed and extended conformations will serve as references for the conformational evaluation of the peptides within the SAMs.

Taking in mind the information gathered from the exploratory simulations of the peptides in solution, their subsequent behavior when approaching the surface was studied by simulating 1, 2 and the gradient ∂ of **IS·Au** and **IPS·Au** immobilized onto the surface first in MeOH, then in water. Starting with the shorter and hydrophobic **IS·Au** in MeOH medium, the <RMSD> of its backbone revealed the same profile as for the free peptide (**ISH** in MeOH) presenting large fluctuations (7.3 ± 3.5 Å for **IS·Au**) demonstrating that structural changes persisted even when the peptide is chemisorbed onto the metal surface. Interestingly, the <RMSD> slightly increases (8.4 and 8.2 Å, respectively) with the increasing peptide concentration (**2-IS·Au** and **∂IS·Au**), meaning that they still undergo large conformational changes, yet with lower oscillations (standard deviation, SD of 1.7 and 1.0 Å, respectively).

Reasonably, the presence of two or more peptides mutually influences the adsorption and conformations of the molecules involved in intermolecular interactions. However, H-bonds between the side chains of the peptides sequence were detected only in the ***∂*IS·Au** system with a maximum of 18 % of average occupancy (ASP-ILE, Table S7-2). Consistent results were observed from the simulation in explicit water solvent (Table 1).

Table 1. Average RMSD, Rg and SASA values calculated along the 10 ns MD simulations in MeOH and water for 1, 2 and *∂* of **ISH**, **IPSH**, **IS·Au**, **IPS·Au**, **IS/CS·Au** and **IPS/PS·Au**. The standard deviation is also reported.

	<RMSD>[a]		<Rg>[a]		<SASA>[b]	
	MeOH	Water	MeOH	Water	MeOH	Water
ISH	4.4 ± 0.9	-	6.7 ± 0.8	-	-	-
Extended			8.7			
Closed			5			
IPSH	1.5 ± 0.4		9.8 ± 1.3			
Extended			13.8			
Closed			6.6			
IS·Au						
1	7.3 ± 3.5	8.9 ± 2.2	7.8 ± 0.9	5.7 ± 0.6	1035 ± 98	751 ± 75
2	8.4 ± 1.7	9.4 ± 2.5	12 ± 1.8	7.6 ± 0.5	1920 ± 128	1169 ± 100
∂	8.2 ± 1.0	5.7 ± 0.8	21.4 ± 0.7	20.2 ± 0.2	16466 ± 748	10585 ± 904
IPS·Au						

1	0.8 ± 0.2	1.0 ± 0.3	8.4 ± 1.4	8.4 ± 1.3	994 ± 52	1015 ± 56
2	3.7 ± 0.7	4.3 ± 2.1	11.3 ± 1.4	9.5 ± 1.2	2032 ± 78	1718 ± 84
∂	5.0 ± 0.9	7.3 ± 1.7	21.5 ± 0.5	21.2 ± 0.3	21209 ± 1578	19649 ± 1581
IS/CS·Au						
1	3.5 ± 0.2	6.3 ± 1.7	8.3 ± 0.9	6 ± 0.3	799 ± 73	590 ± 50
2	3.9 ± 0.3	4.8 ± 1.1	8.7 ± 0.4	7.7 ± 0.2	1311 ± 92	1029 ± 70
∂	6.9 ± 1.0	5.4 ± 1.0	22.5 ± 0.7	22.5 ± 0.2	15412 ± 1187	11539 ± 641
IPS/PS·Au						
1	1.8 ± 0.3	1.6 ± 2.5	12.1 ± 0.7	11.3 ± 0.1	1072 ± 17	1056 ± 22
2	6.0 ± 2.4	9.1 ± 2.5	13.8 ± 0.8	15.3 ± 0.9	2122 ± 45	2155 ± 33
∂	5.5 ± 0.4	5.4 ± 1.2	22.7 ± 0.4	23.1 ± 0.2	24879 ± 1171	25298 ± 1751
[a] Å; [b] A^2						

Although the last MeOH snapshot resulted equilibrated, consistent fluctuations persist also when one or two peptides, freer to move, are simulated in water (8.9 ± 2.2 and 9.4 ± 2.5, respectively). On the other hand, the fluctuations of the SAM gradients are visibly attenuated (5.7 ± 0.8 Å, Table 2) upon water solvation, while persist the same H-bonding interactions previously encountered in MeOH solution (ASP-ILE 16 % of occupancy, Table S7-2).

More precise information concerning the conformational aspects derived from the Rg analysis correlated by a visual inspection (Figure S7-2a and Table 2). Having in mind the Rg values of the two identified conformations (Rg = 5.0 Å and 8.7 Å for the closed and extended conformers,

respectively, Table 2), the <Rg> of **1-IS·Au** implies a transition from an upright orientation in MeOH (<Rg> = 7.8 Å) to a more compact conformation in water (<Rg> = 5.7 Å) where the peptide lies on the Au surface (Figure 5a). Similarly, when two or more molecules are confined on the surface (**2-IS·Au** and ***∂*IS·Au**), an extended conformation is observed in MeOH (<Rg> = 12 ± 1.8 and 21.4 ± 0.7 Å, Table 2), while a drastic conformational collapse on the surface is clearly evidenced when simulated in an aqueous environment (<Rg> = 7.6 ± 0.5 and 20.2 ± 0.2 Å for **2-** and ***∂*IS·Au**, respectively, Table 2). These observations are in line with a known tendency of aa or longer polypeptides to strongly physically absorb on metal surfaces. In particular, the simulated gradient displays a disordered organization in MeOH solution, that becomes a perfect semi-spherical aggregation in water. The collapsed conformation calculated for **1-**, **2-** and ***∂*IS·Au** recalls the low degree of surface organization suggested by the WCA values of the corresponding full isocratic SAM (**IS·Au**, entries 4 and 12 Table S2). Afterwards, the solvent accessible surface area (SASA) profile was assessed for the three simulated structures describing the exposed peptide surface as a function of its conformational change along the time (Figure S7-2c). Indeed, SASA nicely correlates with the conformation of free **ISH** as a certain exposed surface associated to the extended conformation (<Rg> = 7.8 and 12 Å for **1-IS·Au** and **2-IS·Au** in MeOH, Table 2) in MeOH, is remarkably decreased in water as a consequence of the conformational change to the closed arrangement (<Rg> = 5.7 and 7.6 Å, Table 2 and Figure S7-2c). In particular, a drastic reduction of SASA is observed for ***∂*IS·Au** that passes from 16466 to 10585 A^2 from MeOH to water, confirming the disordered aggregation with a reduced surface exposition. This might be at the base of the poor cellular motogenitcity of ***∂*IS·Au**. Further, the electrostatic surface potential both in MeOH and water, displayed in Figure 5a-c, shows the tangential adsorption of the

immobilized Au-peptide pointing the hydrophobic residues (blue coloration) ILE and GLY towards the surface, while exposing the hydrophilic aa (red coloration) GLN or ASP to the solvent bulk (MeOH and water, respectively). This is in line with the low WCA observed experimentally (entries 4 and 12 Table S2), typical of a hydrophilic surface.

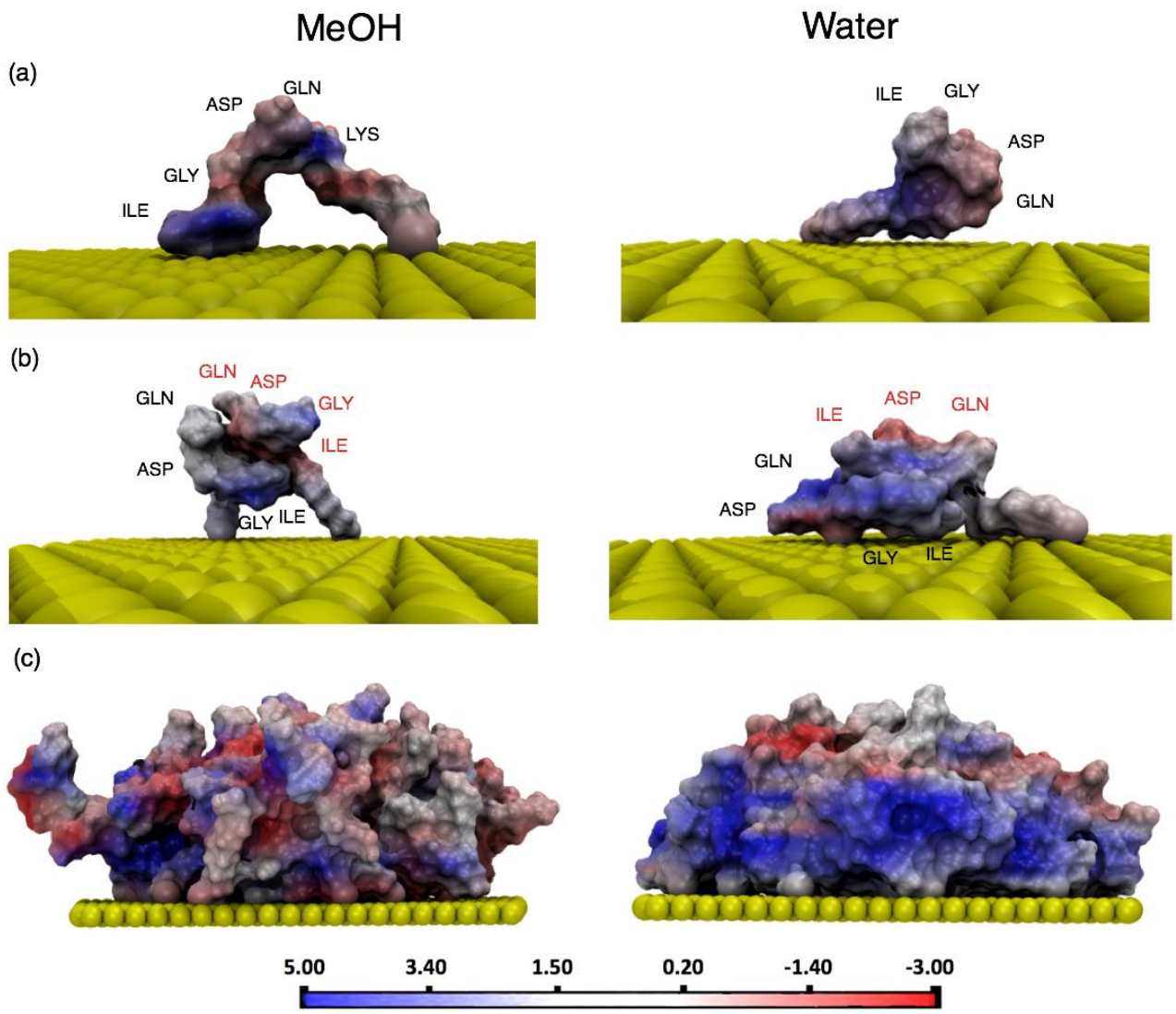

Figure 5. Front views of electrostatic surface potential plotted onto the peptide in the last snapshot of **1-IS·Au** (a), **2-IS·Au** (b), and ***∂*IS·Au** (c) MD simulations in MeOH (left column) and water

(right column). The scale bar at the bottom is also reported. The aa residues within the peptide structures (a and b) are labeled with their symbol name, namely Isoleucine (ILE), Glycine (GLY), Aspartic acid (ASP), Glutamine (GLN) and Lysine (LYS).

Additionally, it is worth noting that the ILE is here the N-term residue, and this could in principle contribute to the binding to Au through the NH_3^+ functional group, known to strongly interact with Au surfaces. The simulated systems demonstrate that the intrinsic backbone flexibility of **ISH** lasts even when the peptide is chemisorbed on Au (high <RMSD>). This is once again translated in the alternation of closed/extended conformations in MeOH (<Rg> values with higher SD with respect to water), while the water environment further favors internal H-bonding interactions to be established, inducing the formation of the closed conformation of one or more collapsing peptides on the metal surface. This explains the reduced SASA values for the water-simulated systems that maximize the contact with the surface rather than the sequence exposition. The expected self-assembly ordering, in principle driven by van der Waals (vdW) interactions among the alkyl linkers, here drastically fails yielding to the spontaneous peptide adsorption on Au through a backbone direct contact. Eventually, the electrostatic surface potential gives a precise mapping of the residues orientation that, mostly pointing the hydrophobic residues towards the Au surface, is in line with the physical (WCA) and functional (biological response) responses caused by the presence of conformationally-folded peptide.

MD simulations were therefore performed on **1-**, **2-** and ***∂*IPS·Au** in order to provide structural insights on the behavior of the hydrophilic peptide once chemisorbed on the Au surface. As observed for the comparison between free **ISH** in solution and that chemisorbed on the metal

surface, the calculation of the <RMSD> reveals that also **IPS·Au** maintains the same stable trend as **IPSH** in MeOH (0.8 ± 0.2 Å for **IPS·Au**, Table 2 and Figure S7-3). Similarly to its equivalent in solution, intramolecular H-bonds are detected, confirming the stable RMSD profile of **IPS·Au** (ASP-GLN 24 % of occupancy, Table S7-2). By increasing the number of peptides (**2-** and **∂IPS·Au**), an effect on the fluctuation of the systems is observed as higher <RMSD> values are calculated (3.7 ± 0.7 and 5.0 ± 0.9 Å for **2-IPS·Au** and **∂IPS·Au**, Table 2). This suggests that conformational rearrangements are occurring when two or more peptides are in contacts although with very small oscillations (low SD values). As expected, the increase of the peptide concentration in the system reveals an increase in the intermolecular interactions, as demonstrated by the large number of H-bonds detected for **2-IPS·Au** (ASP-ILE 33 % of occupancy for intra and intermolecular interactions, Table S7-2) and **∂IPS·Au** (ASP-ILE 99 % of occupancy, Table S7-2). The simulations run in water confirmed the same trend showing **1-IPS·Au** stably fluctuating around a constant RMSD value (1 ± 0.3 Å), which increases as a function of the number of peptides in the systems (4.3 ± 2.1 and 7.3 ± 1.7 Å for **2-IPS·Au** and **∂IPS·Au**, Table 2). Specifically, the fluctuations are now slightly more evident as the <RMSD> are higher in water with respect to the same systems in MeOH (Table 2). In parallel, the H-bonds detected present lower % of occupancy with respect to the simulations in MeOH, especially for the systems with one or two peptides (ASP-GLN from 24 to 8 % of occupancy in **1-IPS·Au**, ASP-ILE from 33 to 0 % in **2-IPS·Au**, Table S7-2). Hence the slight increase in fluctuation (higher RMSD) can be explained by the likewise decrease of occupancy of the observed H-bonds. Information about the conformation of **IPSH** chemisorbed on the surface derives once more from the Rg analysis. Molecular system **1-IPS·Au**, both in MeOH and water, displays an average value of 8.4 Å corresponding to a

conformation in between the folded (Rg = 6.6 Å) and extended (Rg = 13.8 Å) system. On the other hand, **2-IPS·Au** and ***∂*IPS·Au** seem to adopt conformation closer to the extended arrangement, as their <Rg> values range from 11.3 ± 1.4 to 9.5 ± 1.2 Å for **2-IPS·Au** and 21.5 ± 0.5 and 21.2 ± 0.3 for ***∂*IPS·Au** in MeOH and water, respectively. If during the simulations in MeOH, **1-**, **2-** and ***∂*IPS·Au** tend to stand vertical on the surface (first column Figures 6a-c) yet entertaining intra and intermolecular contacts (H-bonds in Table S7-2) one can see that their structures are in an intermediate conformation. On the other hand, when simulated in water the peptides clearly adhere to the metal surface through their backbone (second column Figures 6a-c). Hence in line with the Rg values, the peptides are "extended" but laid down on the surface. Additionally, the electrostatic surface potential reveals that when the peptides adsorb on the surface they mainly point the hydrophobic residues (ILE and GLY) towards the metal while the hydrophilic (ASP and GLN) are solvent-oriented (Figure 6).

Consistently, this nicely correlates with the measured WCA and the high wettability originating from the hydrophilic peptide (entry 3 Table S2). As previously observed, the SASA helps in quantifying the exposition of the peptides chemisorbed onto the surface depending on the adopted conformations. While for **1-IPS·Au** the exposed surface is constant both in MeOH and in water consistently with unvaried Rg (Table 2), in **2-** and ***∂*IPS·Au** a remarkable reduction of the SASA was observed when passing from MeOH to water, consistently with the peptides adhesion to the surface and the reduced exposed surface. The **IPSH** tendency to form H-bonds, as detected from the simulation of **IPSH** in water, may thus be the key factor in modulating the peptide conformation and consequently, upon chemisorption onto Au, its solvent orientation. Inter and

intra-peptide H-bonds are indeed observed during the simulation of **1-**, **2-** and **∂IPS·Au** systems both in MeOH and in water inducing the bending of its structure and the subsequent collapsing onto the surface.

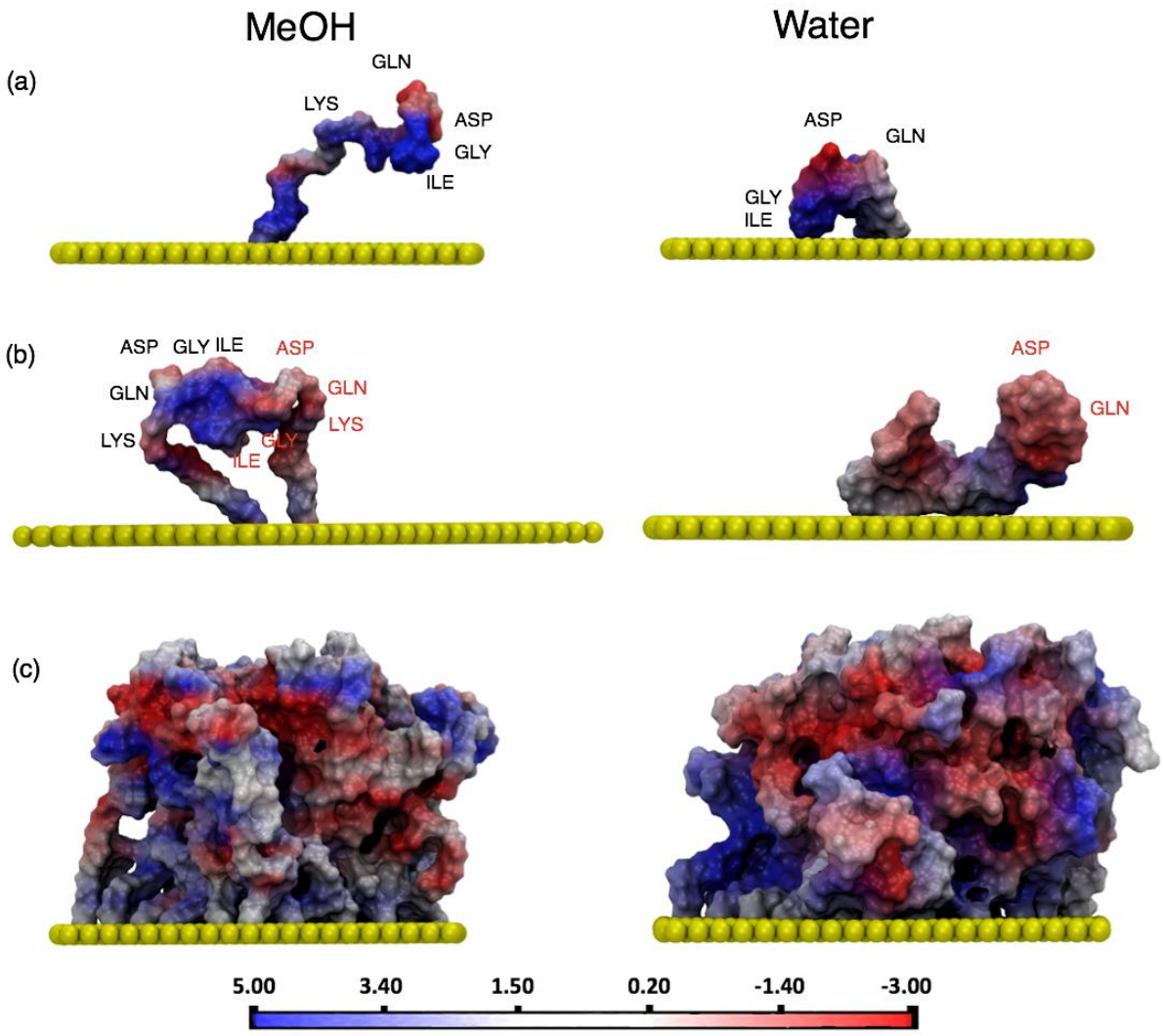

Figure 6. Front view of electrostatic surface potential plotted on the last snapshot of the **1-** (a), **2-** (b) and **∂ IPS·Au** (c) MD simulations in MeOH (left column) and water (right column). The scale

bar at the bottom is also reported. The aa residues within the peptide structure are labeled with their symbol name, namely Isoleucine (ILE), Glycine (GLY), Aspartic acid (ASP), Glutamine (GLN) and Lysine (LYS). The scale bar at the bottom is also reported.

This is accompanied by significant reduction of SASA and major exposition of the hydrophilic residues towards the solvent bulk. In the view of achieving a well-organized and effective motogenic patterned surface, two-components SAMs of **IS·Au** backfilled with the hydrophobic **CSH** molecular filler were successfully produced and tested. Hence, the systematic computational investigation includes also MD simulations of the **1-**, **2-** and **∂IS/CS·Au** systems in MeOH and water, respectively representing the conditions occurring during the surface assembly and biological assessments. When the behavior of the peptide surrounded by the SAM of **CS·Au** is simulated in MeOH, **IS·Au** at any concentration (1, 2 and ∂) displays always drastically dumped fluctuations in the <RMSD> with respect to the isocratic systems (3.5, 3.9 and 6.9 Å respectively, Table 2 and Figure S-4b), which find explanations in the structural organization of the SAM induced by the presence of the filler. Moreover, in **2-IS/CS·Au** the inter-peptide interaction between ASP-LYS comes into occur with an average % of occupancy equal to 6% that increases up to 23% in **∂IS/CS·Au**, along with many other H-bonding pairs (Table S7-2).

When the three systems are then switched to water, the <RMSD> values are generally higher, confirming the high conformational freedom of the peptides within the **IS/CS·Au** SAMs. Notably, these systems maintain the dynamicity of the exposed motogenic sequence emerging from the SAMs, but at the same time conserve the ability of entertaining inter-peptide interactions. For example, in **2-IS/CS·Au** the GLN-GLN H-bonding pair is encountered with 15 % of average

occupancy; whereas in ***∂*IS/CS·Au** the network of H-bonds is expanded as a function of the concentration of the peptide, displaying, among the most occupied H-bonding pairs, the ASP-ASP (30%) and the ASP-ILE pairs (16%, Table S7-2).

Noteworthy, the observed H-bonds are now occurring preferentially between the same residues of different peptides (GLN-GLN or ASP-ASP) assuming a 'face-to-face' reciprocal peptides orientation, prompting any distortion or bending of the peptide structures yet aiding its vertical exposition. This latter hypothesis was then corroborated by the Rg calculated values (Table 2 and Figure S7-4a). The **1-IS/CS·Au** system shows slightly higher <Rg> values compared to **1-IS·Au** (8.3 and 7.8 Å respectively), but with the big difference that the first is actually extended towards the solvent (Figure 7a), the second, although refers to an extended conformation (8.7 Å for **ISH/MeOH**), corresponds to a closed and poorly exposed arrangement (Figure 5a). Moving to water, despite the <Rg> of **1-IS/CS·Au** decreases to 6 Å, the majority of the sequence is still stretched towards the solvent clearly exposing the hydrophobic ILE residue as the electrostatic surface potential reveals (Figure 7a). Similarly, the <Rg> value of **2-IS/CS·Au** simulated in MeOH of 8.7 Å effectively corresponds to the extended conformations and the ideal ILE exposition is maintained (Figure 7b). However, when the system is simulated in water, the two molecules tend to lie on the SAM surface (Figure 7b). This can be explained by the reported tendency of aa such as LYS and GLN that, although polar, bearing a long alkyl side chains, can establish hydrophobic interactions with alkanethiol SAM,[73] as can occur with our CS·Au SAM. Nevertheless, in **1-IS/CS·Au** and **2-IS/CS·Au** a better exposition and readability of the motogenic sequence is now achieved as the hydrophobic ILE are visibly pointing towards the solvent (Figure 7a-b). When it

comes into the evaluation of the peptide exposition in the gradient **∂IS/CS·Au**, it is worth noting that the <Rg> in MeOH is significantly higher than that of the isocratic one component peptide SAM (22.5 and 21.4 Å, respectively), and it remains unvaried also in the simulation in water (22.5 and 20.2 Å respectively, Table 2). Finally, a reduction of <SASA> is recorded at any peptide concentration (1-, 2- and ∂) passing from MeOH to water, from two- to one-component SAMs (Table 2), in principal implying a reduced exposed peptide surface in **IS/CS·Au** systems. However, taking into account that in the **IS·Au** systems the exposed surface is intrinsically higher due to the absence of the surrounding surface fillers, the <SASA> values are surprisingly similar when compared to the two-components systems. In particular, <SASA> of **∂IS·Au** and **∂IS/CS·Au** in MeOH are 16466 ± 748 and 15412 ± 1187 A^2, and in water 10585 ± 904 and 11539 ± 641 A^2, respectively. This suggests that the **CSH** filler effectively ameliorates the peptide exposition as compared to the one-component attempts.

Summarizing, neither the peptide conformation nor the inter-peptide interactions affect the exposition of **IS·Au** when is surrounded by a **CS·Au** SAM in **1-** and **2-IS/CS·Au** as it perfectly exposes its sequence, pointing especially the hydrophobic ILE towards the solvent bulk (both in MeOH and water, Figure 7a-b). When the peptide concentration increases (**∂IS/CS·Au**) it was proved a general major peptide surface exposition (Rg and SASA values) thanks to the contribution of 'face-to-face' H-bonds occurring especially at the base of the peptides. Therefore, *in silico* results agree with the empirical data collected from the WCA measurements and biological tests in revealing the effective capacity of the **CSH** filler in enhancing the peptide availability and sequence exposition.

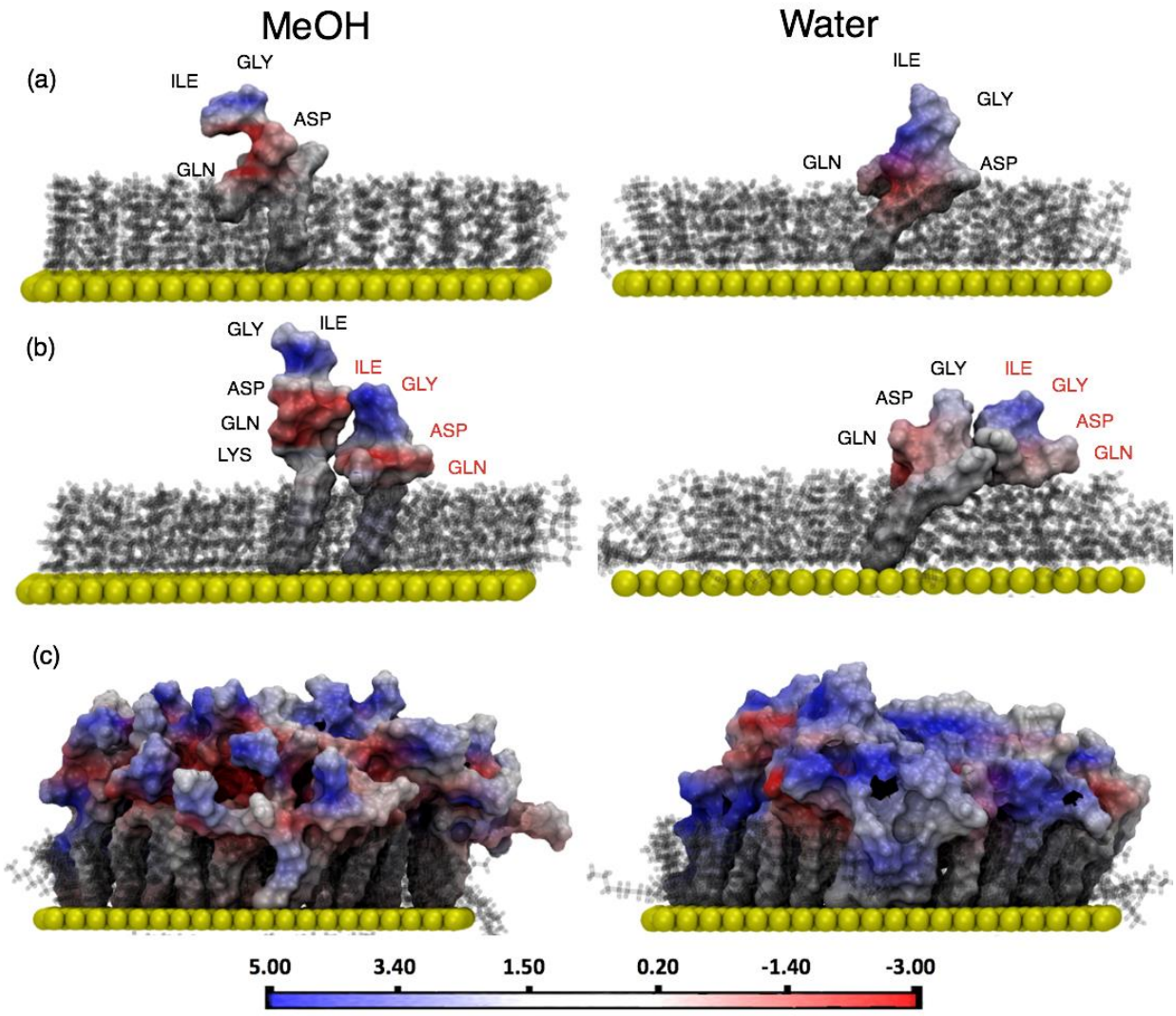

Figure 7. Front view of electrostatic surface potential plotted on the last snapshot of the **1-** (a), **2-** (b) and ***∂*IS/CS·Au** (c) MD simulations in MeOH (left column) and water (right column). The scale bar at the bottom is also reported. The aa residues within the peptide structure are labeled

with their symbol name, namely Isoleucine (ILE), Glycine (GLY), Aspartic acid (ASP), Glutamine (GLN) and Lysine (LYS). The scale bar at the bottom is also reported.

Finally, the comprehension of the behavior of the experimentally tested SAMs was completed by performing the same simulations and analysis also on **1-**, **2-** and ***∂*IPS/PS·Au**. Surprisingly the <RMSD> of all the simulated systems surrounded by the hydrophilic filler are now slightly increased in values with respect to the corresponding one-component SAMs, both in MeOH and in water (Table 2 and Figure S11). A proper look at the intra and intermolecular interactions explains the faint increase in <RMSD> with the decrease, up to the complete loss, of occupancy of the previously observed H-bonds (for example ASP-GLN from 24 to 18 % of occupancy in MeOH, from 8 to 0 % in water for **1-IPS·Au** and **1-IPS/PS·Au**, respectively, Table S7) which reasons the higher peptide freedom and flexibility.

In parallel, during the water simulations the ASP-PEG H-bonding pair starts appearing with an occupancy of 10 % for **1-IPS/PS·Au** and of 15 % for **2-IPS/PS·Au**. This might represent an anchoring point of the peptides to the surrounding filler SAM that simultaneously prevents the IPS peptides from bending and/or stacking among each other. As a proof of this, the MeOH <Rg> values remarkably range close to the extended conformation (12.1 and 13.8 Å for **1-IPS/PS·Au** and **2-IPS/PS·Au**, respectively) as well as in water (11.3 and 15.3 Å for **1-IPS/PS·Au** and **2-IPS/PS·Au**, Table 2 and Figure S11). Significantly, in the gradient system the anchoring occurs between LYS, the linking residue at the base of IGDQK peptide, and the adjacent PEGs (about 70 % and 56 % of occupancy in MeOH and water, respectively Table S7-2). The latter completes the intricate network of H-bonds that is also observed for the ***∂*IPS/PS·Au** system which explains the

stable and reduced <RMSD> values compared to the one-component system (Table 2). The anchoring LYS-ASP interactions along with the 'face-to-face' residues H-bonding seems guarantying the extended conformation also during the gradient simulations recording an increase in <Rg> from 22.7 to 23.1 Å passing from MeOH to water. The quantification of the peptide exposition was also in these cases assessed by the SASA measurements in perfect agreement with the conformational analysis. **1-** and **2-IPS/PS·Au** present higher exposed surface with respect to the one-component systems (Table 2). Importantly, <SASA> values are unvaried passing from MeOH to water (Table 2) in line with the similar conformation observed in the last snapshot of the simulations (Figure 8a-b) where one can appreciate the precise orientation of each residue. Blue coloration associated to the ILE residue is clearly pointing toward the solvent for **1-IPS/PS·Au** especially in MeOH (Figure 8a). In **2-IPS/PS·Au**, the peptide-filler intermolecular interactions suffice in separating the two IPS that, unaffected by their contacts, can properly and correctly expose the sequence starting with the hydrophobic portion of ILE and GLY (Figure 8b). Finally, ***∂*IPS/PS·Au** uncovers higher surface compared to ***∂*IPS·Au** in MeOH (24979 and 21209 A^2, respectively) that significantly increases in water instead of decreasing as previously observed (25298 and 19649 A^2, Table 2). The extended conformation associated to such exposition is then evident in Figure 8c.

The problem on how similar surfaces perform so differently as experimentally observed, was also taken on by means of classical MD simulations focusing on the three main variables that constitute the systems: the IGDQ-peptides, the surface fillers and Au. The comprehension at the atomistic level of details regarding their way of mutually interact between and among them reveals

interesting aspects that explain the behavior of such IGDQ peptide adsorbed on Au and correlate with the biological activities.

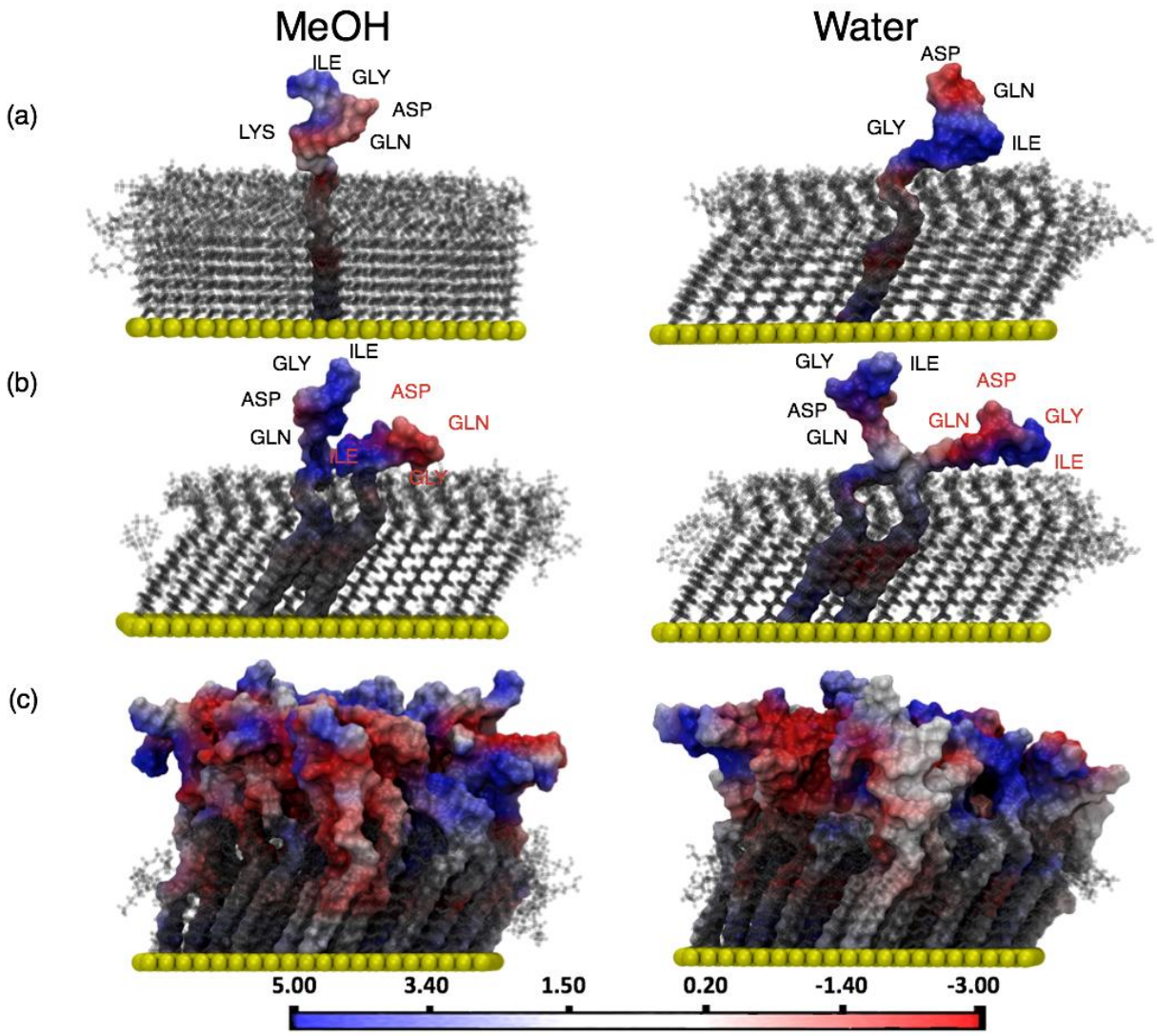

Figure 8. Front view of electrostatic surface potential plotted on the last snapshot of the **1-** (a), **2-** (b) and ***∂*IPS/PS·Au** (c) MD simulations in MeOH (left column) and water (right column). The scale bar at the bottom is also reported. The aa residues within the peptide structure are labeled

with their symbol name, namely Isoleucine (ILE), Glycine (GLY), Aspartic acid (ASP), Glutamine (GLN) and Lysine (LYS). The scale bar at the bottom is also reported.

One of the first evidence pointed out by the computational results is that, regardless the hydrophobic (**ISH**) or hydrophilic (**IPSH**) nature of the peptides, the IGDQ portion spontaneously and directly interacts with the Au surface. The high **ISH** flexibility in one-component SAMs overreaches closed conformation stabilized by intermolecular H-bonds that bending the peptide backbone, points the hydrophobic portion of the peptide on Au while exposing to the solution the hydrophilic ones (Figure 9a). The same results are achieved by one-component **IPSH** SAM, now due to its ability to entertain intramolecular H-bonds (Table S7-2) which results in the predominantly hydrophilic SAM, as observed in Figure 9b. These findings are at the base of the failure of both ***∂*IS·Au** and ***∂*IPS·Au** in attaining an organized, ordered and ultimately effective motogenic SAM, as evidenced by the WCA values of these systems and the equivalent gradients presenting also the surface fillers.

On the other hand, the second important finding revealed by the computational studies is the modality through which the fillers achieve organized and motogenic surfaces. Remarkably, in the two-components SAM gradient **IS/CS·Au** the peptides conformation is now more extended most likely thanks to the presence of **CSH** filler that, aiding the extended conformation, favors 'face-to-face' H-bonds at the base of the peptides, further stabilizing a more hydrophobic SAM as showcased in Figure 9c. Consistently, in two-components **IPS/PS·Au** gradient (Figure 9d) most of the conserved inter-peptides interactions are accompanied by new emerged anchoring points occurring between ASP and PEG from the surrounding hydrophilic fillers (Table S7-2), or 'face-

to-face' H-bonds orientations that sustain the erected peptide conformation from their base. A blue (hydrophobic) coloration is indeed observed in the top view of **∂IPS/PS·Au** provided in Figure 9d.

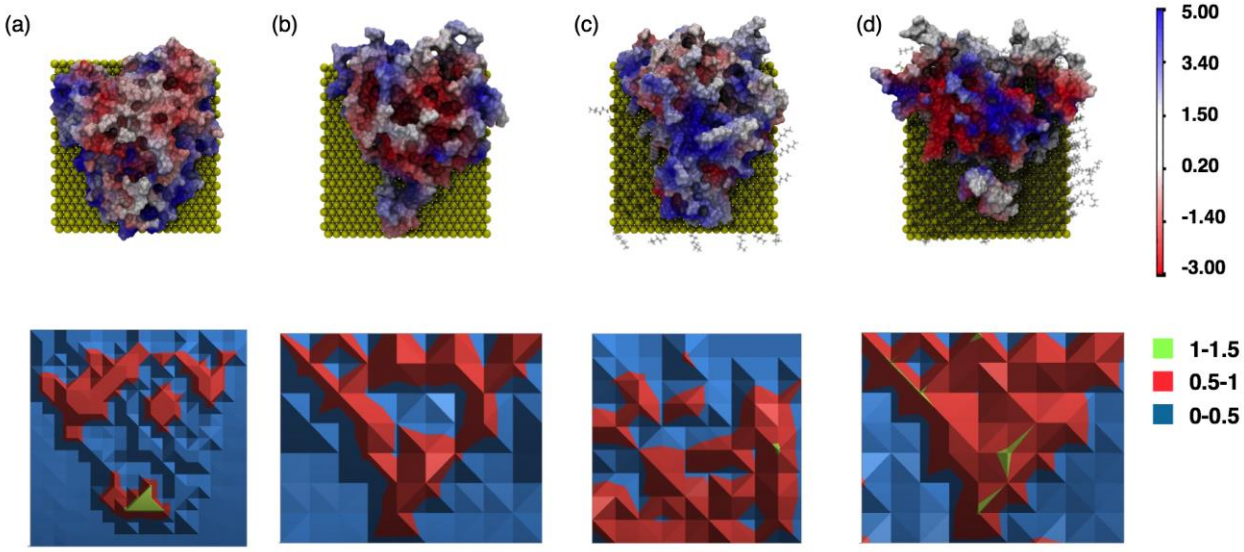

Figure 9. Top view of the electrostatic surface potential plotted on the last snapshot of the **∂IS·Au** (a), **∂IPS·Au** (b) **∂IS/CS·Au** (c) and **∂IPS/PS·Au** (d) MD simulations in water. The scale bar at the side is also reported: blue coloration corresponds to hydrophobic portion, red to hydrophilic ones and bluish/white/reddish describe the situation in between. Bottom: maps generated by calculating the RDFs by residues (terminal ILE of IGDQ, terminal CH_3 of CS and PS, Au atoms) over the 10 ns trajectories at 3.75 Å of distance for **∂IS·Au** (a) **∂IPS·Au** (b) **∂IS/CS·Au** (c) and **∂IPS/PS·Au** (d). From the lowest to the highest water density, each considered residue within the RDF maps are colored in blue, red and green respectively.

However, despite exhaustive and detailed, the analyses carried out so far on the gradient simulated systems do not provide any precise information about the part of the peptide sequence actually

visible and prone to exert the motogenic function. Although the Rg and SASA represent a clear proof of the major sequence stretching and disclosure in **∂IS/CS·Au** and **∂IPS/PS·Au** (Table 2), the correct readability of the sequence remains to be addressed. It is worth recalling that within the IGDQ sequence the ILE acts as pivotal residue for the correct biological recognition and activity,[19] therefore considered the target aa for the readability of our peptide sequence. Aiming at this, the radial distribution functions (RDFs) were calculated only for the gradient systems simulated in water, since it is crucial in the biological test conditions to demonstrate the correct sequence recognition. At first, the RDFs were calculated between the water O and the entire contact surface (Supporting Information S7) thereby defining the distance with the higher water density in the four systems. In order to address the water-peptide interactions as a measure of the sequence exposition to the solvent, the RDFs was calculated for each residue separately at the defined distances (3.25 Å for **∂IS·Au** and 3.75 Å for **∂IS/CS·Au**, **∂IPS·Au**, and **∂IPS/PS·Au**) between the water O and respectively the C of the terminal ILE of the **IS·Au** and **IPS·Au** molecules, the C atom of the terminal methyl group of **CS·Au** and **PS·Au**, and between the water O and the Au atoms when no fillers are present. Doing so it has been possible to measure the patterned surfaces-water interactions and picture a precise and punctual water distribution map over the surfaces (Figure 9, bottom). A RDF map is therefore drawn coloring the ILE, Au and the two fillers according to the relative water density around them, thus the degree of exposition will correspond to low (blue coloration) medium (red) and high (green) water density.

The RDF map of **∂IS·Au** shows a lower water density in correspondence of the gold atoms that, completely covered by the peptides, are indeed not water-exposed (Figure 9a, light blue

coloration). On the other hand, the presence of the peptide defines a distinct solvent density cone, which is barely exposed only where the ILE are oriented towards the solvent (higher exposition red-green coloration), albeit the predominance of the blue coloration still evidences a poor exposition of the ILE residues. Knowing that the ILE exposition is fundamental for the motogenic activity of these patterned surfaces, these findings nicely correlate to the absence of biological response when **∂IS·Au** SAM was tested. The RDF map along with the evident hydrophilicity emerging from the electrostatic surface potential of **∂IS·Au** (Figure 9a) is in perfect agreement with the increase of hydrophilicity along the gradient observed by the wettability assessment (ΔWCA = -4.9°, Table S2).

Similarly, the RDF map of **∂IPS·Au** displays low water density in correspondence of the gold surface, most likely due to its peptide coverage, while the well-defined IPS cone is only slightly more solvent exposed (red coloration) with considerable holes going from the lower to the higher peptide concentration (blue coloration, Figure 9b). The areas of the RDF map in which the ILE is poorly solvent exposed well match the hydrophilic spots revealed by the electrostatic surface potential, describing a situation in which to the increasing concentration of the peptide does not correspond the ILE exposition, thereby possible explanation of the devoid motogenicity of **∂IPS·Au**.

On the other hand, the RDF map of **∂IS/CS·Au** displays a diffused red coloration, a clear sign of the water exposition of both CS and ILE residues progressively exposed as a function of the peptides concentration (Figure 9c). The MD simulation shows that this patterned surface remarkably exposes the ILE residues therefore yielding a hydrophobic surface as observed in the

blue coloration of the electrostatic surface potential (Figure 9c, top). These results are in line with the experimental WCA values that unveil a significant variation in polarity along the gradient (ΔWCA = 22.5°, entry 10 Table S2). Hence, the remarkable motogenic activity of the gradient **IS·Au** backfilled with **CS·Au** is explained by the correct orientation of the motogenic sequence, starting with ILE, as demonstrated by this *in silico* validation.

Finally the RDF map of ***∂*IPS/PS·Au** unambiguously shows a red-green coloration at the peptide cone level which starts with the less peptide concentrated area and persist up to the highest concentrated ones (Figure 9d). Of note, the surrounding PS filler is blue colored implying that its terminal methyl group is not solvent exposed probably covered by the adjacent peptides. The proper ILE exposition is thus verified also for the ***∂*IPS/PS·Au** for which effective motogenic activity was indeed registered (Figure 4).

In conclusion, the RDF map was herein used as valuable and suitable analysis to precisely elucidate at the atomistic level the polarity of the produced SAMs correlating with the experimental WCA measurements. By punctually quantifying the ILE readability along the different gradients, through the RDF maps we were able to confirm the structural-activity relationship ultimately clarifying the divergent biological responses of the produced SAMs. Therefore, the hydrophilicity of ***∂*IS·Au** can be ascribed to the insufficient ILE orientation towards the water (Figure 9a), which reasonably causes no motogenic response of cancer cells deposited on such surface. The map of the ***∂*IPS·Au** system unveils a negligible increase of the ILE water orientation, which is in agreement with the experimental evidences of a surface that do not suffice to attain cell migration. In the same measure, it was nicely demonstrated that the improved performance of the two components

systems **∂IS/CS·Au** and **∂IPS/PS·Au** in the organization and exposition of the motogenic sequence is essentially due to the major and correct orientation of the ILE residues. Hence their hydrophobic nature, as observed experimentally and computationally, accounts for the exposition of the ILE aa thereby providing effective motogenic surfaces.

CONCLUSIONS

In this study we have employed both experimental and computational approaches for unraveling the structure-activity relationships of a set of synthetic ECM analogues exposing the IGD motifs of Fibronectin. Such small library of substrates exposes the peptide motifs onto hydrophilic or hydrophobic backgrounds, with either an isotropic peptide density (isocratic SAMs), or a surface-imprinted peptide gradient (SAM gradients). The physicochemical characterization of their wettability, surface composition and morphology clearly link the SAM composition (peptide sequence, filler and anisotropicity) with the surface organization, the latter being responsible of the effects at the biological interface. In relation to the cell adhesion properties, hydrophilic IGDQ SAMs are able to trigger a response otherwise missing in the absence of the peptide, suggesting the specificity of this peptide in modulating the cell anchorage onto these substrates. Regarding the motogenicity, only the two-component IGDQ SAM gradients possess the proper combinations of peptide structure, peptide density, and anisotropic composition to correctly expose the IGD sequence at the biological interface, ultimately triggering motogenicity.

The computational analyses reveal how the sum of the interactions occurring at the intra-peptide, inter-peptide, peptide-filler and peptide-Au determines the IGD sequence readability at the biological interface, as a function of the peptide surface density and the presence of the fillers.

Taken together, all this information rationalizes how the observed SAM organization determines not only the peptide conformation, but most likely also its effective readability by a yet unknown biological target, whose effect is the activation of specific cell machineries that participate in the orchestration of the observed long term cell migration. A deeper control of IGD-alkanethiols surface density and their structural modifications might be the future routes toward a more efficient modulation of the whole-cell population migration, towards metastatic cancer cells phenotypization and sorting.

ASSOCIATED CONTENT

Supporting Information. Detailed SAMs preparation, cell seeding, and xurography protocols, along with computational analyses are available free of charge

SupportingInfo.pdf

AUTHOR INFORMATION

Corresponding Author

*bonifazid@cardiff.ac.uk

Author Contributions

F.D.L. performed the theoretical simulations, R.M. and V.C. performed all the experiments and actively participated in the discussion and development of the project. S.S. provided all the xerographic surfaces. D.B. supervised and coordinated all project, fed the main ideas and wrote the manuscript together will all authors. All authors have given approval to the final version of the manuscript.

Funding Sources

D.B. gratefully acknowledges the EU through the ERC Starting Grant "COLORLANDS, the Science Policy Office of the Belgian Federal Government (BELSPO-IAP 7/05 project), the EU for the ITN FINELUMEN project and Cardiff University. R.M. thanks the FRS-FNRS for his post-doctoral fellowship.

ACKNOWLEDGMENT

F.D.L. and D.B. gratefully acknowledge Prof. A. De Vita, Dr. M. Riello and Dr. G. Doni for the fruitful discussions on the computational settings.

ABBREVIATIONS

CCR2, CC chemokine receptor 2; CCL2, CC chemokine ligand 2; CCR5, CC chemokine receptor 5; TLC, thin layer chromatography.

REFERENCES

1. Kim, H. D.; Peyton, S. R. Bio-inspired materials for parsing matrix physicochemical control of cell migration: A Review. *Integr. Biol.* **2012,** *4* (1), 37-52.
2. Bonnans, C.; Chou, J.; Werb, Z. Remodelling the extracellular matrix in development and disease. *Nat. Rev. Mol. Cell. Biol.* **2014,** *15* (12), 786-801.
3. Mouw, J. K.; Ou, G.; Weaver, V. M. Extracellular matrix assembly: A multiscale deconstruction. *Nat. Rev. Mol. Cell. Biol.* **2014,** *15* (12), 771-785.

4. Wong, I. Y.; Javaid, S.; Wong, E. A.; Perk, S.; Haber, D. A.; Toner, M.; Irimia, D. Collective and individual migration following the epithelial–mesenchymal transition. *Nat. Mater.* **2014,** *13* (11), 1063-1071.
5. Friedl, P.; Gilmour, D. Collective cell migration in morphogenesis, regeneration and cancer. *Nat. Rev. Mol. Cell. Biol.* **2009,** *10* (7), 445-457.
6. Mosher, D. F.; Adams, J. C. Adhesion-modulating/matricellular ECM protein families: A structural, functional and evolutionary appraisal. *Matrix Biol.* **2012,** *31* (3), 155-161.
7. Brooks, A. N.; Kilgour, E.; Smith, P. D. Molecular pathways: Fibroblast growth factor signaling: A new therapeutic opportunity in cancer. *Clin. Canc. Res.* **2012,** *18* (7), 1855-1862.
8. Pollak, M. The insulin and insulin-like growth factor receptor family in neoplasia: An update. *Nat. Rev. Cancer* **2012,** *12* (3), 159-169.
9. Shibuya, M. Vascular endothelial growth factor and its receptor system: Physiological functions in angiogenesis and pathological roles in various diseases. *J. Biochem.* **2013,** *153* (1), 13-19.
10. Alberts, B.; Johnso, A.; Lewis, J.; Raff, M.; Roberts, K.; P. Walter. *"Molecular Biology of The Cell- 4th ed."*; Garland Science

New York, 2002.
11. Carsons, S. E. The structure and function of Fibronectins. In *Fibronectin in Health and Disease*, Carsons, S. E., Ed.; CRC Press Inc.: Florida, 1989, p Ch. 1.
12. Akiyama, S. K.; Olden, K.; Yamada, M. Fibronectin and integrins in invasion and metastasis. *Canc. Metastasis Rev.* **1995,** *14* (3), 173-189.
13. Pierschbacher, M. D.; Ruoslahti, E. Cell attachment activity of fibronectin can be duplicated by small synthetic fragments of the molecule. *Nature* **1984,** *309* (5963), 30-33.
14. Ruoslahti, E.; Pierschbacher, M. D. New perspectives in cell adhesion: RGD and integrins. *Science* **1987,** *238* (4826), 491-497.
15. Ruoslahti, E. RGD and other recognition sequences for integrins. In *Annual Review of Cell and Developmental Biology*, 1996; Vol. 12, pp 697-715.
16. Ma, H.; Hao, J. Ordered patterns and structures via interfacial self-assembly: Superlattices, honeycomb structures and coffee rings. *Chem. Soc. Rev.* **2011,** *40* (11), 5457-5471.
17. Love, J. C.; Estroff, L. A.; Kriebel, J. K.; Nuzzo, R. G.; Whitesides, G. M. Self-assembled monolayers of thiolates on metals as a form of nanotechnology. *Chem. Rev.* **2005,** *105* (4), 1103-1169.
18. Zhang, S. Fabrication of novel biomaterials through molecular self-assembly. *Nat. Biotech* **2003,** *21* (10), 1171-1178.
19. Schor, S. L.; Ellis, I.; Banyard, J.; Schor, A. M. Motogenic activity of IGD-containing synthetic peptides. *J. Cell Sci.* **1999,** *112* (22), 3879-3888.
20. Houard, X.; Germain, S.; Gervais, M.; Michaud, A.; Van Den Brûle, F.; Foidart, J. M.; Noël, A.; Monnot, C.; Corvol, P. Migration-stimulating factor displays HEXXH-dependent catalytic activity important for promoting tumor cell migration. *Int. J. Canc. Res.* **2005,** *116* (3), 378-384.

21. Yang, S. T.; Liu, Y.; Wang, Y. W.; Cao, A. Biosafety and bioapplication of nanomaterials by designing protein-nanoparticle interactions. *Small* **2013,** *9* (9-10), 1635-1653.
22. Gray, J. J. The interaction of proteins with solid surfaces. *Curr. Opin. Struct. Biol.* **2004,** *14* (1), 110-115.
23. Di Felice, R.; Corni, S. Simulation of peptide-surface recognition. *J. Phys. Chem. Lett.* **2011,** *2* (13), 1510-1519.
24. Corvaglia, V.; Marega, R.; De Leo, F.; Michiels, C.; Bonifazi, D. Unleashing Cancer Cells on Surfaces Exposing Motogenic IGDQ Peptides. *Small* **2016,** *12* (3), 321-329.
25. De Leo, F.; Sgrignani, J.; Bonifazi, D.; Magistrato, A. Structural and dynamic properties of monoclonal antibodies immobilized on CNTs: a computational study. *Chem. Eur. J.* **2013,** *19* (37), 12281-93.
26. De Leo, F.; Magistrato, A.; Bonifazi, D. Interfacing proteins with graphitic nanomaterials: from spontaneous attraction to tailored assemblies. *Chem. Soc. Rev.* **2015,** *44* (19), 6916-53.
27. Pineux, F.; Marega, R.; Stopin, A.; La Torre, A.; Garcia, Y.; Devlin, E.; Michiels, C.; Khlobystov, A. N.; Bonifazi, D. Biotechnological promises of Fe-filled CNTs for cell shepherding and magnetic fluid hyperthermia applications. *Nanoscale* **2015,** *7* (48), 20474-88.
28. Stopin, A.; Pineux, F.; Marega, R.; Bonifazi, D. Magnetically Active Carbon Nanotubes at Work. *Chem. Eur. J.* **2015,** *21* (26), 9288-301.
29. Marega, R.; Bonifazi, D. Filling carbon nanotubes for nanobiotechnological applications. *New J. Chem.* **2014,** *38* (1), 22-27.
30. Roberts, C.; Chen, C. S.; Mrksich, M.; Martichonok, V.; Ingber, D. E.; Whitesides, G. M. Using Mixed Self-Assembled Monolayers Presenting RGD and (EG)3OH Groups To Characterize Long-Term Attachment of Bovine Capillary Endothelial Cells to Surfaces. *J. Am. Chem. Soc.* **1998,** *120* (26), 6548-6555.
31. Chen, S.; Cao, Z.; Jiang, S. Ultra-low fouling peptide surfaces derived from natural amino acids. *Biomaterials* **2009,** *30* (29), 5892-5896.
32. Chelmowski, R.; Köster, S. D.; Kerstan, A.; Prekelt, A.; Grunwald, C.; Winkler, T.; Metzler-Nolte, N.; Terfort, A.; Wöll, C. Peptide-based SAMs that resist the adsorption of proteins. *J. Am. Chem. Soc.* **2008,** *130* (45), 14952-14953.
33. Yousaf, M. N. Model substrates for studies of cell mobility. *Curr. Opin. Chem. Biol.* **2009,** *13* (5-6), 697-704.
34. Mrksich, M. Dynamic substrates for cell biology. *MRS Bull.* **2005,** *30* (3), 180-184.
35. Lee, E. J.; Luo, W.; Chan, E. W. L.; Yousaf, M. N. A molecular smart surface for spatio-temporal studies of cell mobility. *PLoS ONE* **2015,** *10* (6), e0118126.
36. Nowinski, A. K.; Sun, F.; White, A. D.; Keefe, A. J.; Jiang, S. Sequence, structure, and function of peptide self-assembled monolayers. *J. Am. Chem. Soc.* **2012,** *134* (13), 6000-6005.
37. Boncheva, M.; Vogel, H. Formation of stable polypeptide monolayers at interfaces: Controlling molecular conformation and orientation. *Biophys. J.* **1997,** *73* (2), 1056-1072.
38. Holle, A. W.; Young, J. L.; Spatz, J. P. In vitro cancer cell-ECM interactions inform in vivo cancer treatment. *Adv. Drug Deliv. Rev.* **2016,** *97*, 270-279.

39. Luo, W.; Westcott, N.; Dutta, D.; Pulsipher, A.; Rogozhnikov, D.; Chen, J.; Yousaf, M. N. A Dual Receptor and Reporter for Multi-Modal Cell Surface Engineering. *ACS Chem. Biol.* **2015,** *10* (10), 2219-2226.
40. Mrksich, M. Using self-assembled monolayers to model the extracellular matrix. *Acta Biomaterialia* **2009,** *5* (3), 832-841.
41. Hong, G.; Heinz, H.; Naik, R. R.; Farmer, B. L.; Pachter, R. Toward understanding amino acid adsorption at metallic interfaces: A density functional theory study. *ACS Appl. Mater. Interfaces* **2009,** *1* (2), 388-392.
42. Heinz, H.; Farmer, B. L.; Pandey, R. B.; Slocik, J. M.; Patnaik, S. S.; Pachter, R.; Naik, R. R. Nature of molecular interactions of peptides with gold, palladium, and Pd-Au bimetal surfaces in aqueous solution. *J. Am. Chem. Soc.* **2009,** *131* (28), 9704-9714.
43. Ghiringhelli, L. M.; Hess, B.; Van Der Vegt, N. F. A.; Delle Site, L. Competing adsorption between hydrated peptides and water onto metal surfaces: From electronic to conformational properties. *J. Am. Chem. Soc.* **2008,** *130* (40), 13460-13464.
44. De Roe, C.; Courtoy, P. J.; Baudhuin, P. A model of protein-colloidal gold interactions. *J. Histochem. Cytochem.* **1987,** *35* (11), 1191-1198.
45. Hnilova, M.; Oren, E. E.; Seker, U. O. S.; Wilson, B. R.; Collino, S.; Evans, J. S.; Tamerler, C.; Sarikaya, M. Effect of molecular conformations on the adsorption behavior of gold-binding peptides. *Langmuir* **2008,** *24* (21), 12440-12445.
46. Verde, A. V.; Acres, J. M.; Maranas, J. K. Investigating the specificity of peptide adsorption on gold using molecular dynamics simulations. *Biomacromolecules* **2009,** *10* (8), 2118-2128.
47. Serr, A.; Horinek, D.; Netz, R. R. Polypeptide friction and adhesion on hydrophobic and hydrophilic surfaces: A molecular dynamics case study. *J. Am. Chem. Soc.* **2008,** *130* (37), 12408-12413.
48. Tamerler, C.; Duman, M.; Oren, E. E.; Gungormus, M.; Xiong, X.; Kacar, T.; Parviz, B. A.; Sarikaya, M. Materials specificity and directed assembly of a gold-binding peptide. *Small* **2006,** *2* (11), 1372-1378.
49. Bellucci, L.; Brancolini, G.; Calzolari, A.; Parramon, O. C.; Corni, S.; Di Felice, R. Proteins and peptides at gold surfaces: Insights from atomistic simulations. In *ACS Symposium Series*, 2012; Vol. 1120, pp 229-250.
50. Yu, J.; Becker, M. L.; Carri, G. A. The influence of amino acid sequence and functionality on the binding process of peptides onto gold surfaces. *Langmuir* **2012,** *28* (2), 1408-1417.
51. Hoefling, M.; Monti, S.; Corni, S.; Gottschalk, K. E. Interaction of β-sheet folds with a gold surface. *PLoS ONE* **2011,** *6* (6), e20925.
52. Leufgen, K.; Mutter, M.; Vogel, H.; Szymczak, W. Orientation modulation of a synthetic polypeptide in self-assembled monolayers: A TOF-SIMS study. *J. Am. Chem. Soc.* **2003,** *125* (29), 8911-8915.
53. Seigel, R. R.; Harder, P.; Dahint, R.; Grunze, M.; Josse, F.; Mrksich, M.; Whitesides, G. M. On-Line Detection of Nonspecific Protein Adsorption at Artificial Surfaces. *Anal. Chem.* **1997,** *69* (16), 3321-3328.

54. Bain, C. D.; Troughton, E. B.; Tao, Y. T.; Evall, J.; Whitesides, G. M.; Nuzzo, R. G. Formation of monolayer films by the spontaneous assembly of organic thiols from solution onto gold. *J. Am. Chem. Soc.* **1989,** *111* (1), 321-335.
55. Pale-Grosdemange, C.; Simon, E. S.; Prime, K. L.; Whitesides, G. M. Formation of self-assembled monolayers by chemisorption of derivatives of oligo(ethylene glycol) of structure HS(CH2)11(OCH2CH2)mOH on gold. *J. Am. Chem. Soc.* **1991,** *113* (1), 12-20.
56. Morgenthaler, S.; Lee, S.; Zürcher, S.; Spencer, N. D. A simple, reproducible approach to the preparation of surface-chemical gradients. *Langmuir* **2003,** *19* (25), 10459-10462.
57. Nuzzo, R. G.; Allara, D. L. Adsorption of bifunctional organic disulfides on gold surfaces. *J. Am. Chem. Soc.* **1983,** *105* (13), 4481-4483.
58. Prime, K. L.; Whitesides, G. M. Self-assembled organic monolayers: Model systems for studying adsorption of proteins at surfaces. *Science* **1991,** *252* (5009), 1164-1167.
59. Tamada, K.; Nagasawa, J.; Nakanishi, F.; Abe, K.; Ishida, T.; Hara, M.; Knoll, W. Structure and growth of hexyl azobenzene thiol SAMs on Au(111). *Langmuir* **1998,** *14* (12), 3264-3271.
60. Pace, G.; Ferri, V.; Grave, C.; Elbing, M.; Von Hänisch, C.; Zharnikov, M.; Mayor, M.; Rampi, M. A.; Samorì, P. Cooperative light-induced molecular movements of highly ordered azobenzene self-assembled monolayers. *Proc. Natl. Acad. Sci. U.S.A.* **2007,** *104* (24), 9937-9942.
61. Kumar, A. S.; Ye, T.; Takami, T.; Yu, B. C.; Flatt, A. K.; Tour, J. M.; Weiss, P. S. Reversible photo-switching of single azobenzene molecules in controlled nanoscale environments. *Nano Lett.* **2008,** *8* (6), 1644-1648.
62. Song, B.; Chen, K.; Schmittel, M.; Schönherr, H. AFM Study of Surface Nanobubbles on Binary Self-Assembled Monolayers on Ultraflat Gold with Identical Macroscopic Static Water Contact Angles and Different Terminal Functional Groups. *Langmuir* **2016,** *32* (43), 11172-11178.
63. Song, B.; Walczyk, W.; Schönherr, H. Contact angles of surface nanobubbles on mixed self-assembled monolayers with systematically varied macroscopic wettability by atomic force microscopy. *Langmuir* **2011,** *27* (13), 8223-8232.
64. Song, B.; Zhou, Y.; Schönherr, H. Optimized Model Surfaces for Advanced Atomic Force Microscopy Studies of Surface Nanobubbles. *Langmuir* **2016,** *32* (43), 11179-11187.
65. This surface characterization can exploit the structural difference between the peptide alkanethiols and the surface fillers (presence of nitrogen atoms).
66. Morgenthaler, S. M.; Lee, S.; Spencer, N. D. Submicrometer structure of surface-chemical gradients prepared by a two-step immersion method. *Langmuir* **2006,** *22* (6), 2706-2711.
67. Desgrosellier, J. S.; Cheresh, D. A. Integrins in cancer: biological implications and therapeutic opportunities. *Nat. Rev. Cancer* **2010,** *10*.
68. Bökel, C.; Brown, N. H. Integrins in development: Moving on, responding to, and sticking to the extracellular matrix. *Dev. Cell* **2002,** *3* (3), 311-321.
69. An incubation time of 4h was selected as a best compromise to induce both cell adhesion and FAK expression and phosphorylation and discriminate SAMs' adhesiveness.
70. Gabarra-Niecko, V.; Schaller, M. D.; Dunty, J. M. FAK regulates biological processes important for the pathogenesis of cancer. *Cancer Metastasis Rev.* **2003,** *22*.

71. Hsia, D. A.; Mitra, S. K.; Hauck, C. R.; Streblow, D. N.; Nelson, J. A.; Ilic, D.; Huang, S.; Li, E.; Nemerow, G. R.; Leng, J.; Spencer, K. S. R.; Cheresh, D. A.; Schlaepfer, D. D. Differential regulation of cell motility and invasion by FAK. *J. Cell Bio.* **2003,** *160* (5), 753-767.
72. Mitra, S. K.; Schlaepfer, D. D. Integrin-regulated FAK-Src signaling in normal and cancer cells. *Curr. Opin. Cell Bio.* **2006,** *18* (5), 516-523.
73. Taherian, A.; Li, X.; Liu, Y.; Haas, T. A. Differences in integrin expression and signaling within human breast cancer cells. *BMC Cancer* **2011,** *11* (1), 1-15.